Spring 2017

Multifunctional Transition Metal Oxide Core Shell Magnetic Nanoparticles

Mahmud Reaz
Missouri State University, Reaz54@live.missouristate.edu

Follow this and additional works at: https://bearworks.missouristate.edu/theses

Part of the Physical Sciences and Mathematics Commons, and the Structural Materials Commons

Recommended Citation

MULTIFUNCTIONAL TRANSITION METAL OXIDE CORE SHELL

MAGNETIC NANOPARTICLES

A Masters Thesis

Presented to

The Graduate College of

Missouri State University

In Partial Fulfillment

Of the Requirements for the Degree

Master of Science, Materials Science

By

Mahmud Reaz

August 2017

MULTIFUNCTIONAL TRANSITION METAL OXIDE CORE SHELL

MAGNETIC NANOPARTICLES

Physics, Astronomy, and Materials Science

Missouri State University, August 2017

Master of Science

Mahmud Reaz

ABSTRACT

Oxide core-shell nanoparticles (CSNPs) have attracted considerable interest for their multifunctional properties. Luminescent ZnO, ferroelectric BaTiO3, and inverse spinel iron oxide can be exploited to develop magneto-luminescent and multiferroic nanomaterials. The novel sonochemical method has been used to synthesize the nanomaterials. Atomic-scale spectroscopy establishes the core-shell nature and multifunctional properties of the nanomaterials. Magnetic hysteresis (coercivity, remnant, and saturation magnetization) and temperature dependent data indicate the key structural difference between the oxidized and reduced ZnO/iron oxide CSNPs. Variation in the coercive field and remnant and saturation magnetization further confirms the presence of different iron oxides in the shell region. Temperature and field dependent magnetization data establish the change in the near superparamagnetic behavior. Modeling of the X-ray photoelectron spectroscopy data and Rietveld refinement of the X-ray diffraction data provide the crystallographic, surface, and interface information. Photoluminescence data prove luminescence of the ZnO core. Transmission and scanning electron microscopy data confirm the multiferroic BaTiO3/iron oxide core-shell nanospheres important for magnetoelectric coupled devices.

KEYWORDS: transition metal oxides, core-shell nanoparticles, magneto-luminescence, multiferroics, X-ray photoelectron spectroscopy, X-ray diffraction data, magnetic properties.

This abstract is approved as to form and content

_____
Kartik Ghosh, PhD
Chairperson, Advisory Committee
Missouri State University

MULTIFUNCTIONAL TRANSITION METAL OXIDE CORE SHELL

MAGNETIC NANOPARTICLES

By

Mahmud Reaz

A Masters Thesis
Submitted to the Graduate College
Of Missouri State University
In Partial Fulfillment of the Requirements
For the Degree of Masters of Science, Materials Science

August 2017

Approved:

_____

Kartik Ghosh, PhD, Chairperson

_____

David Cornelison, PhD, Member

_____

Mahua Biswas, PhD, Member

_____

Keiichi Yoshimatsu, PhD, Member

_____

Julie Masterson, PhD: Dean, Graduate College

ACKNOWLEDGEMENTS

TABLE OF CONTENTS

LIST OF TABLES

LIST OF FIGURES

INTRODUCTION

Nanomaterials

Recently, nanomaterials are widely investigated by researchers from the field of engineering (computer and electronic) and the physical sciences (physics, chemistry, biology, electrical, computer and materials sciences). Small to the gigantic devices and instruments rely on materials properties at the atomic scale. Nanoscale materials are the key for approaching the major global problems related to energy, electronic, and biomedical engineering. Confinement in at least two or more spatial dimensions gives rise to the unique optical, magnetic, electric, thermal and mechanic properties. Physical properties tuning through critical surface/ interface studies in the multifunctional composite/core-shell nanostructures allow the possibility of combining distinct materials functionality.

History. Functional nanomaterials have been a part of our environment from the start. Foraminifera, protein, capsid, wax crystals on lotus or nasturtium, spider milk, blue hue tarantulas are few of many nanomaterials exists in nature(Hudson et al., 2013). Multiple monolayers are responsible for the magnificent color of the Blue Tarantula. Use of functional nanomaterials in steel can be dated back to 500 AD in Damascus (History and Development of Nanomaterials). Nanomaterials were also used in Mesopotamia culture around 900 BC for creating a glittering effect on surface pots (Nanotechnology Timeline | Nano). Nanomaterials have become increasingly important in modern technology since the discovery of scanning tunneling microscope in the 1980s. Fullerene discovery was a breakthrough in the first decade. The early 2000s was the beginning of the nanotechnology commercialization. It has been seen the widespread use of nanomaterials from biomedical to aerospace engineering. The discovery and groundbreaking research on graphene (resulted in 2010 Noble Physics Noble Prize) were

a significant breakthrough in this decade. In 2011, a group of astronomers using Spitzer Space Telescope claimed the detection of fullerene and graphene in space (NASA - Honeycomb Carbon Crystals Possibly Detected in Space). In today's cross-cutting era of technology, nanomaterials are the key to vary the structure-property dependence in quantum scale. Nanomaterials promise improvement in electronics, biomedicine, drug delivery, self-cleaning surfaces, cosmetics, disinfectant, structural materials in aerospace and much more.

Properties. Materials of spatial dimension 1 μm or higher give constant physical properties irrespective of the sizes and shapes. As the size approaches the nanoscale (less than 100 nm), surface properties are no longer negligible to the bulk. High surface to volume ratio creates novel physical properties. Quantum confinement changes the physical properties so much that most materials bulk and nano properties are incompatible.

<u>Optical Properties.</u> Electronic confinement changes the valence band and the conduction band energies significantly. Electron transition between the two states is responsible for the materials emission and absorption spectrum. It is possible to change the emission and absorption spectra of the nanoscale materials (NPs and quantum dots) through varying the size and shape. Optical property is highly correlated with the electronic, magnetic and thermal properties and is of utmost importance for the nanomaterials. Optical properties such as color, absorbance, and luminescence of the semiconductors and many metals are a function of the NP size. Tuning the optical properties is vital for the optical detector, laser, sensor, imaging, phosphor, display, solar cell, photo catalysis, photo electrochemistry and biomedicine(Zhang, 2006). Doping, coating and surface environment have an influence on the optical properties along with the size and shape morphologies. UV-VIS, photo and electro

luminescence, time-resolved, nonlinear, and single NPs/ molecule spectroscopy are some of the widely-used techniques to probe the NP optical properties (Zhang, 2009).

Electronic Properties. Modern technology already uses electronic gates of 50 nm dimensions or lower. As spatial dimension approaches the de Broglie wavelength of the system, quantum mechanics phenomena dictate over the classical one. Discrete nature of the energy spectrum no longer remains negligible. Conductivity changes due to the increasing wave-like nature of the electrons. Below the critical length scale, some materials start behaving as an insulator. E.g., change in the STM tip conductance is a useful example essential for spectroscopy applications. Nano-electro-mechanical systems based on the electronic responses in the nanoscale is the research area of increasing interest for automotive industries. Nanocrystals and nanomaterials in the range of Fermi wavelength have shown unique mechanical and electronic properties. E.g., carbon nanostructures show a wide variety of unique electrical-electronic property and high chemical stability (Salaheldeen Elnashaie et al., 2015). Quantum effects allow transistors to operate on a scale of single electron tunneling to amplify current (Salaheldeen Elnashaie et al., 2015). Coupling between the electron density and electromagnetic wave in the dielectric-metal interface makes plasmatic nanomaterials crucial for energy to health applications.

Magnetic Properties. The magnetic NPs response depends on a magnetic field. Nanobeds or nanochain magnetic response differs from the bulk counterpart. Higher magnetic susceptibility, generally found in nanoscale superparamagnetic materials, is a desirable property for the magnetic sensors and devices switching applications. Magnetic NP consists of a magnetic material with a functional component. The larger surface area makes the NPs reactive and increases the ability to attach a functional group. Magnetic NPs can be

synthesized using various methods such as chemical synthesis, thermal decomposition, microwave, and template-assisted synthesis, magnetic assembly, and sonochemical synthesis. Magnetic NPs are particularly important for fluids recording, catalysis, biotechnology, electrochemical sensing, memory devices, magnetic resonance imaging (MRI), and supercapacitor electrode(Khan et al., 2014).

Core-Shell Nanostructures. Unique structural feature consisting of a distinct core and shell makes core-shell nanoparticles (CSNP) to achieve multifunctional properties. It received incredible research interest in recent years exhibiting the improved and tailorable materials properties.

Transition Metal Oxides

Transition metal oxides (TMO) are highly abundant materials in earth's crust and found in the various form. One major challenge of the condensed matter physics is to understand the strongly correlated (electron) TMO. Inorganic oxide materials and interfaces are thermodynamically stable for device applications. They are an active material of interest in electronics, physics, chemistry, and materials science. Since the development of pulsed laser deposition techniques in 1987, the field of oxide materials research has grown at an incredible pace (Venkatesan, 2014). TMOs are particularly interesting due to some unique and tunable electronic, optical and magnetic properties. High electron correlation insides the TMO structure results in the neighbor-dependent properties. Electrons are no longer remains in a sea and there is no single theory (LDA/ Hartee-folk) which can describe the behavior of all the transition metals. Competing charge, spin, and structural degrees of freedom result in varying superconducting, superionic, spintronic, and catalytic properties. Many times, synthesis

parameters play a key role in shaping materials structure and properties. While some of the potentials of TMOs are well known, it is a yet discoverable field from many aspects.

TMOs have applications in many fronts including transparent electronics, photonics, optoelectronics, magneto-electronic, spintronic, thermoelectric, and piezoelectric (Lorenz et al., 2016). Photonic materials are special for their possible use in quantum computers, lasers, LEDs, solar cell, imaging, and materials processing. Magnetic materials are important in rotors, magnetic resonance imaging (MRI), memory devices, targeted drug delivery system, magnetic field sensors, and magnetic semiconductors. In addition, magnetic and optical materials are ideal systems for studying fundamental sciences. Coupling between strong ferromagnetic and ferroelectric materials opens the door for the next generation magneto-electric coupled sensors and devices.

Luminescence. The transition of electrons and holes between the energy states yields the luminescence. Large band gap TMOs like ZnO and Ti Fe_2O_3 have grown considerable interest due to the wide emission spectrum in the visible band. Luminescence in these oxides traces back to the several structural defects. While phosphor materials contain one or more impurity sites, nanostructures of ZnO and Ti Fe_2O_3 can produce luminescence from the intrinsic defects. Nanostructured materials create larger surface area and hence logarithmically increases surface defects. Surface oxide layers in the transition metals have been investigated extensively and differ significantly from the bulk band diagram (Baraldi, 2008). The technologically important luminescent material must have stable emission and reproducibility of the results. Luminescent nanomaterials will significantly contribute in lamps, targeted drug delivery, and bioimaging systems.

Wide-band gap ZnO is well studied for the laser, LED, diode, and semiconductor device based applications (Rodnyi and Khodyuk, 2011). It is also the most researched TMO phosphors and yet no theory conclusively reveals the origin of the defect states in the PL spectrum. Models and the experiments often contradict each other than agreement. The presence of more than 10 defect sites and their subsequent modification with size, shape, surface reactivity and chemical environment makes the ZnO luminescence significantly tunable. Low toxicity and biodegradability make ZnO suitable for nano-bio applications (Zhang et al., 2013). ZnO NP with a magnetic nanocomposite/coating can modify the structure for the targeted drug delivery, cell labeling with external magnetic field, magnetic resonance imaging and bio-imaging based applications (Rasmussen et al., 2010). Understanding and optimizing the luminescence property can contribute to design a multifunctional ZnO material to fulfill the technological demand of the coming era.

Magnetism. Magnetic NPs are a class of materials responsive to the influence of magnetic fields. TMO structure exhibits a wide range of changes in magneto-resistance and superconductivity in the nanoscale (Brink, 2006). Metal oxygen bonding in the TMO varies from nearly ionic, metallic, to highly covalent (Rao, 1989). Diversity in the electronics structure exhibits ferromagnetic (Cr Fe_2O_3, $La_{0.5}Sr_{0.5}MnO_3$), ferrimagnetic (Υ-Fe_2O_3, 3O4, $Y_3Fe_{15}O_{12}$), superparamagnetic (Fe_3O_4, Υ-Fe_2O_3), and antiferromagnetic (NiO, $LaCrO_3$) properties (Rao, 1989). Iron oxide is an especial magnetic material found in 16 forms. Two prominent magnetic oxides of all time are magnetite (Fe_3O_4) and maghemite (Υ-Fe_2O_3). Bulk magnetite and maghemite are both ferromagnetic in nature. Superparamagnetic responses in these materials been observed once constraint (2nm to 20nm) in spatial dimensions (Bu, 2016). Fe_3O_4 and Υ-Fe_2O_3 are of prime interest due to their biocompatibility, conjugation with

bio-tissues, memory device applications, and MRI contrast agent capability. Besides, non-toxicity and biocompatibility make iron oxide stand out for applications in the targeted drug carriers, MRI, gene carriers, magnetic sensing probes, neoadjuvant for vaccine and antibody production (Bu, 2016).

Magneto-Luminescent Oxide NPs

Magneto-luminescent (ML) oxide NPs are stable, multifunctional, and mostly inert to functional ligands. Some of the applications include cell and tissue labeling, controlled delivery (drug and gene), bio-detection (proteins, pathogen, and DNA structures), tissue engineering, hyperthermia, and MRI contrast agent. Biocompatible ML CSNP already delivered antigen into bio cells (Cho et al., 2011). Typical route of designing ML CSNP would include a magnetic core with the luminescent coating. However, the scope of varying the magnetic response is often limited to this structure. Luminescent coating restricts varying magnetic property through surface treatment. Magnetically tuned CSNP increases the possibility of producing better results with some of the existing technology. Understanding the science in the magnetic and luminescence oxide interfaces is essential to design the next generation multifunctional materials.

Multiferroics. Coexistence of the ferromagnetic, ferroelectric, and ferroelastic ordering in the multiferroic materials promises for the more compact devices and sensors for the future. Polarization (Magnetic/ electric) through external field (Electric/ magnetic) is known as magneto-electric effect. Magneto-electric materials are expected to be implemented in the micro-electromechanical system (MEMS & NEMS), data storage media, spintronic, spin valves, non-volatile, random access memories (Zhao and Shifeng, 2015). Multiferroic NP has interesting applications such as magnetic tweezers, protein and DNA separators,

therapeutic agents for hyperthermia, MRI contrast agent, radioactive isotopes for radio and chemotherapy(Kargol et al., 2012). Nanomaterials functional surface and cross coupling between magnetic and dielectric states make core-shell multiferroic nanostructure ideal for high-tech applications.

Magneto-Electric Oxide NPs

Magneto-electricity is first mentioned in the 1959 edition of Landau & Lifshitz' *Electrodynamics of Continuous Media*. Multiferroic materials experienced a surge of interests since 2000. The Science behind the multiferroic materials behavior holds present technological importance. Magnetoelectric coupling through field -polarization interaction promises the development of advanced spintronic, sensors, memory, and magnetic semiconductor based device applications. Magnetoelectric (ME) effect so far been observed in thin films, heterostructures, ferrite composites, transition metals, alloys (Sreenivasulu et al., 2014), and CSNP. Theoretical calculation shows the favorability of strong ME coupling in ferromagnetic-ferroelectric core-shell nanostructures (particles, pillars, and wires).

ML ZnO-IRON OXIDE CSNP SYNTHESIS, CHARACTERIZATION, AND OPTIMIZATION

Abstract

Tailoring the magnetic properties like coercivity, remnant and saturation magnetization make the CSNPs suited for biomedical applications. We report tunable magnetic properties of magneto-luminescent ZnO/iron oxide core-shell nanoparticles (CSNPs) made using sonochemical synthesis technique. Annealing the sample in N_2-H_2 and Ar-H_2 ambient changes the magnetic property within the inverse spinel space group (Fd$_3$m) sustaining ZnO luminescence intact. Successful structural changes between maghemite (γ-Fe_2O_3) and its reduced form magnetite (Fe_3O_4) have been identified in the shell. Following the method discussed in this article, CSNPs is tunable for both hard and soft magnet based applications. Detailed surface and interface studies through XRD, XPS, Raman, SEM, TEM, and PL provides the structure-property correlation necessary to understand the system.

Introduction

Size-dependent magneto-luminescent NPs becoming increasingly important for bioimaging, drug delivery, cancer treatment, and hyperthermia. Iron Oxide/ ZnO CSNP is a widely-researched nanostructure of the last decade. Varying the superparamagnetic coating can increase the efficacy of ML NPs. The fixed magnetic response of NPs has already been successfully used in bio-applications. Current technology relies on a magnetic core with luminescence coating. Magnetic coating on the surface allows the NPs for further treatment to tune the magnetic characteristics as per requirement. Reduced ZnO/Iron oxide CSNP shows variability in the coercive field, remnant magnetization, and saturation magnetization.

Coexistence of the luminescent property in the core region is crucial to preserve the parallel bio-imaging accessibility of the NPs.

Methods

Chloride and Nitride solution forms NPs/nanoclusters on their own. Iron oxide is known to form in the acidic solution under forced hydrolysis (Wang et al., 2008). Nanoscale ZnO is a piezoelectric material with significant surface defect and charge. Intricate defect-rich ZnO NP surface incorporates iron ions in the aqua solution. ZnO surface and properties are overly sensitive to synthesis methods and reaction conditions. Quantum effects are experimentally evident on 10-15 nm particles or less. ZnO NP sonochemically dispersed in $FeCl_3.6H_2O$ + DDI water solution physiochemically coats the NP with 0.5-3 nm coating. Probe sonication for an hour disperses and coats the NP uniformly. We used the reagent grade N_2 flushed $FeCl_3.6H_2O$ and ZnO NPs from Acros Organics and Stream Chemicals
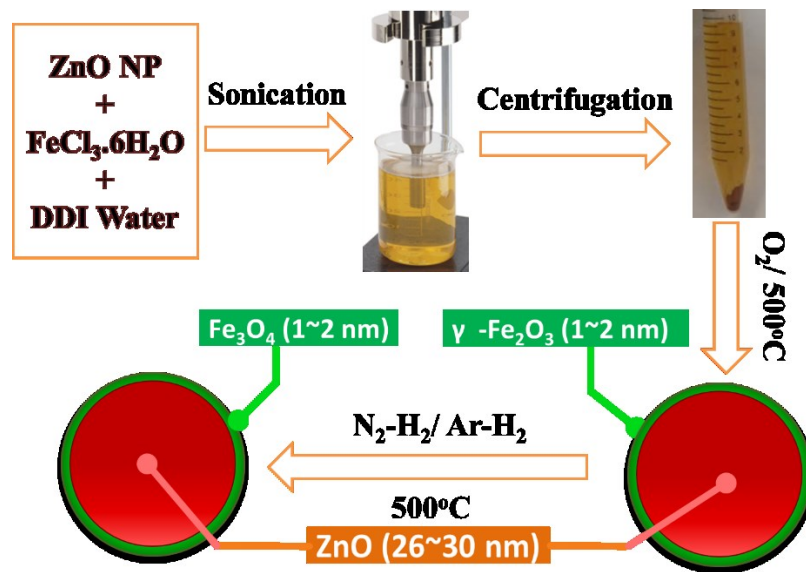
Figure 1: Core-Shell NPs Synthesis Procedure

respectively. As a solvent and cleaning agent, we used DDI water (18MΩ). Every tool and vile used during the process is cleaned using DI water, Methanol, Isopropanol, Acetone and dry N_2 purge. ZnO NPs and FeCl3.6H_2O were mixed in an aqua solution at 2:1 weight ratios. FeCl3.6H_2O dissolves in water while NP is not soluble and precipitates quickly. Block diagram in Fig. 1 shows the synthesis and control parameters. CSNP synthesis is consists of three major parts. First, the sonication of the sample for an hour to enables monodispersing. This allows the physio-absorption of iron, hydroxyl, and chloride ions to take place on NP surface. Second, 30 minutes' centrifugation for few times separates NPs from the remaining FeCl3 solution. Finally, 500^0C oxidation (two hours) of the precipitates in the ambient atmosphere produces the iron oxide structure over ZnO surface. Reduction of the developed ZnO/iron oxide CSNP in either N_2-H_2 / Ar2-H_2 ambient changes maghemite (Υ-Fe_2O_3) crystallographic phase to magnetite (Fe_3O_4). All the samples have been oxidized in atmospheric pressure and reduced in 5×10^{-3}mbar around 500^0C.

High-quality sub-nm resolution nanoscale imaging depends on the dispersion of the NPs. Imaging of a conglomerated individual oxide NPs is challenging with a single beam SEM. Accelerating voltage (15kV to 30kV) excites the K-lines of the materials of interest (Zn, Fe, and Fe_2O_3) for identifying the element concentrations (Wuhrer and Moran, 2016). Intrinsic, extrinsic, and surface defects prevent ZnO and iron oxide being ideal insulators. Constant 5 mm distance for SEM imaging and 12 mm distance for performing EDS analysis gave all the images and phase percentages. The gold coating is not necessary, as the sample is conductive enough. Image resolution and number of secondary electrons generated is directly dependent on spot size. Lower spot size increases clarity at higher magnification. Smaller spot

size causes gaps in the signals and larger spot size averages the overlapped signal. The spot size of 20 nm and 60 nm during the SEM imaging and EDS quantification worked perfectly. Dwell points does not change upon changing the magnification. 20-30 μs dwell time is suitable for over 200000x magnification. Plasma etched sample surface reduced organic contamination. Analysis of SEM-EDS images and data provides particle size distribution as well as elemental information. Methanol improved dispersion while we have tried to disperse the NP with the other alcohols like heptane, methanol, and ethanol. Flat Si substrate offers a much-improved contrast in comparison with Pt, Cu, and Al.

Transmission Electron Microscopy (TEM) is unparalleled in providing sub-nm resolution imaging as well as elemental mapping. Electron lensing and wide-angle spherical aberrations along with small-angle diffraction effects compromise the TEM performance. Resolution d (equation 1) depends on the spherical aberration coefficient of the objective lens (C_S), and electron wavelength(λ) and it is given by equation 1(Smith, 2015),

$$d = A C_s^{\frac{1}{4}} \lambda^{\frac{3}{4}} \dots \dots \dots \dots \dots \dots \dots \dots (1)$$

Where A is a constant (0.43 to 0.7) depending on the type of imaging (coherent, incoherent, or phase contrast). A beam of electrons (100 to 1250 keV) passes through the thin specimen to produce the image. Quantitate interpretation also relies on specimen thickness, composition, orientation, structural defects, and thermal vibrations (Petrova, 2006). High-angle annular dark-field imaging (HAADF) STEM imaging using atomic number (Z) contrast provides till 2 Å lateral resolution (Petrova, 2006). The electron of 200 to 300 keV energy produces near atomic scale resolution during the line scan across the surface/interface region. In HAADF, energy-dispersive X-ray spectroscopy (EDX) data depend on the incoherently scattered electrons and provide the atomic composition and topography. TEM-EDX probes

the core-shell nature of the NPs at sub-nm resolution. Half an hour methanol sonication disperses the NP. Immediate drop cast on Cu-C grid ensures a minimum conglomeration of the NPs on the substrate. 80^0C drying and subsequent plasma etching prepares the samples for best possible imaging and quantitate analysis. To verify the uniformity and the core-shell nature of the nanostructure- line, and area scan data along the core, shell, and interface play a key role.

X-ray diffraction (XRD) is an analytical technique for quantitatively determining crystallographic phase information. XRD provides the fingerprint of a crystalline material. It also provides percent crystallinity of the phases. X-ray wavelength is of the same order of the atomic spacing inside the crystals. Due to the persistent atomic spacing and the periodicity in the crystalline structure, a collection of atoms behaves like a grating to the incident X-rays. The reflected X-rays forms a diffraction pattern revealing phase, occupancy, and unit cell parameters. For less than 1nm crystals, peak broadening makes the crystal phase undetectable in most of the standard diffractometers. Crystal structure of a single phase around the nm scale is detectable in some cases with a slow scan. For our samples, phase mixture of the 25nm to 1-2 nm scales makes SP detection challenging. Moreover, isolated nano particulates give relatively strong signal than the shell region. During the acquisition of XRD data, two things can happen. First, nano-particulates can suppress the signal coming from the shell. Second, due to the enormously low thickness, signals from the shell may be inseparable from the background when there are no particulates. To overcome these problems, it is of high importance to check the drawn conclusion with the complementary techniques such as the X-ray photoelectron spectroscopy (XPS) and superconducting quantum interference device (SQUID) measurement.

XRD technique is useful for determining the molecular structure of the CSNP. Vacuum grease glues the CSNP to a glass substrate for XRD measurement. The state of the art LYNXEYE detector on a Bruker D8 Discover diffractometer measures the XRD data using Cu radiation. The scan conditions were a step width of 0.008° at a measuring time of 5sec per step from 2θ angle 20^0 to 80^0. The total scan time taken was roughly 10 hours. Crystallographic Information Framework data of Fd_3m (γ-Fe_2O_3), Fd_3m (Fe_3O_4) and $P_{63}mc$ (ZnO) space-group structure from ICSD and COD database help perform the refinement. Raw data from the X-ray Diffractometer has been analyzed using Topas (Bruker) Rietveld refinement (Rietveld and IUCr, 1969).

$$M = \sum_i W_i\{(y_i(obs) - y_i(cal)\}^2 \dots\dots\dots\dots\dots\dots\dots (2)$$

Rietveld analysis minimizes Rietveld refinement difference function (Rietveld and IUCr, 1969) given in equation-2 by varying the structural parameters. It matches the theoretical and experimental structural data by approximating the ideal structure. It considers the characteristics of the beam, the experimental arrangement, and the detector setting. The peak position, broadening, and symmetry analysis gives information on particle size, strain, phase, lattice parameter, impurity, thermal agitation, crystallinity, and quantitative presence. Often nano scale materials peaks overlap and shift due to broadening and strain. The virtual separation between the peaks in the Rietveld refinement is suitable for TMO nanopowder diffraction. Glass background from the data been subtracted using Origin Pro 8.5.

For photo-luminescent measurement, the sample has been excited with an energy (325-nm UV-laser source) above the bandgap of a material. Horiba LabRam detects the defect emission through a CCD detector. The visible beam splitter splits the light coming from the sample by wavelength. Tungsten carbide substrate contributes almost no signal to the sample.

Methanol sonicated sample drop cast on SiC substrate produces minimum background for the PL measurement. Time and acquisition averaged data invalidate the contribution from the random noises. Spike and denoise filter further minimize the noises at room temperature.

Quantum Design SQUID magnetometer produces the temperature and field dependent magnetization data from low temperature as low as 2K to 300K. A drinking straw (a lightweight homogeneous plastic tube) as a sample tube minimizes background noises and stray effects. Collective background from the capsule and sample tube was measured and found insignificant to the sample data. Thus, original data with background looks suitable for comparison.

XPS measures empirical formula, chemical state, electronic state, and elemental composition. The advantage of the XPS is that it can quantitatively detect all element from the Lithium (Li) and above. Most of the photoelectron contributing to the detector comes from a sample depth of 5nm or less. It is the finest technique for probing CSNP surface/ interface. XPS is analogous to the SEM/EDS except it requires an ultra-high vacuum condition, and in XPS, high energy X-ray irradiates the samples than accelerating electrons in SEM/EDS. It is possible to simulate the shell thickness of uniform dispersed nanospheres. Conglomeration, non-uniform thickness, and the presence of particulates pose a challenge to match the simulated data with the experimental one. The discontinuity from the bulk make the surface layers (1nm) more reactive to the incoming ray. This is partly because atoms on all sides do not surround surface atoms. Al Kα X-ray source irradiates the sample with an energy of 1486.6 eV. The lower and upper bound of the kinetic energy values is 100 and 1300 eV, respectively. Aperture value remains constant throughout the measurement.

Results and Discussion

SEM images in Fig. 2 show acceptable separation between the iron oxide coated ZnO elliptical NP on a Si substrate. Yellow scales are drawn on top of every image to comprehend the particle sizes. Scale length for all the four quadrants is given in the top left corner of the Fig. 2a shows the CSNP annealed in the N_2-H_2 ambient. Further analysis (only measuring the major axis of the ellipse) in ImageJ provides a size
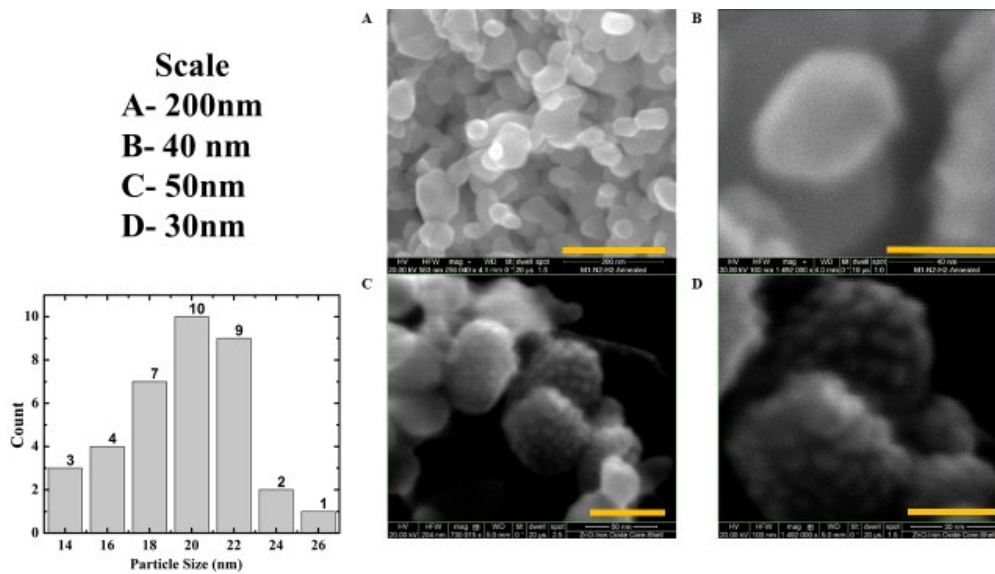
Figure 2: SEM picture showing (a, b) -N_2+H_2 Annealed (c, d)- Fe_2O_3 Annealed

distribution (Fig. 2) around 20 nm. Fig. 2b shows the dimension of one individual NP. Fig. 2 a, b confirms the presence of the ZnO in spherical/elliptical NPs form. Fig. 2c, d shows the cubic nanoislands on the Fe_2O_3 annealed CSNP surfaces. The presence of these islands originates from the incomplete coating over NPs surface. However, these islands were not reproducible in other trials. Fig. 3a represents the region of interest for TEM imaging and analysis. The colored elemental mapping of Zn, Fe, and (Zn+Fe) atoms is presented in Fig. 3b, c, d respectively. Fig. 3b points to the uniform presence (high contrast) of the Zn atoms except
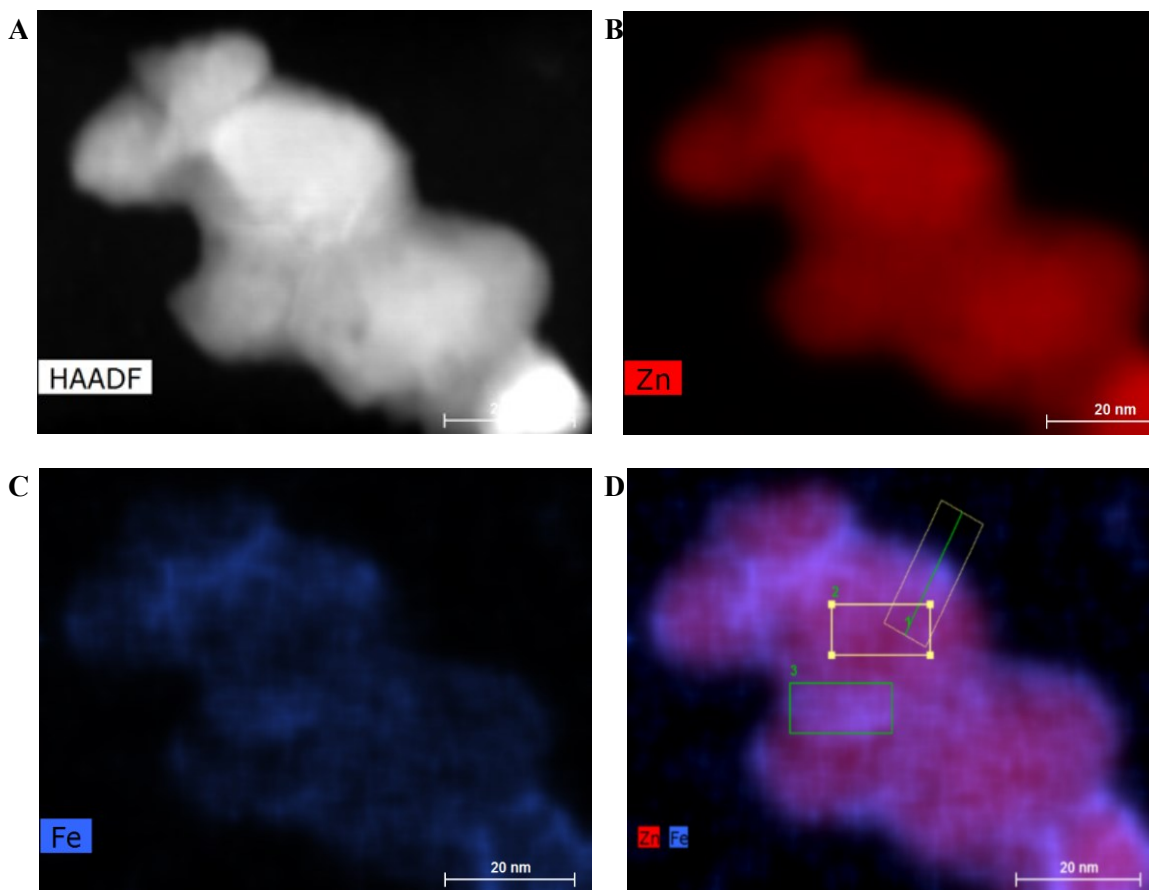
Figure 3: TEM picture showing (a) imaging area (b) Zn Atom only (c) Fe Atom Only (d) Zn and Fe atom combined

for the surfaces and interfaces (faded color). Fig. 3b, c is incompatible in a sense that the later shows the higher presence of the Fe atoms in the surface/interface. Fig. 3d visually indicates that the Zn intensity remains constant throughout the core and falls intensely in the shell. The larger longitudinal cross-sectional area of the iron oxide near surface increases Fe count significantly. Quantitative analysis across the yellow line (Fig. 4a, b) shows that the Fe and Zn atom counts increases and decreases around the 12 nm distance respectively. TEM data is reproducible and in the agreement between multiple attempts.
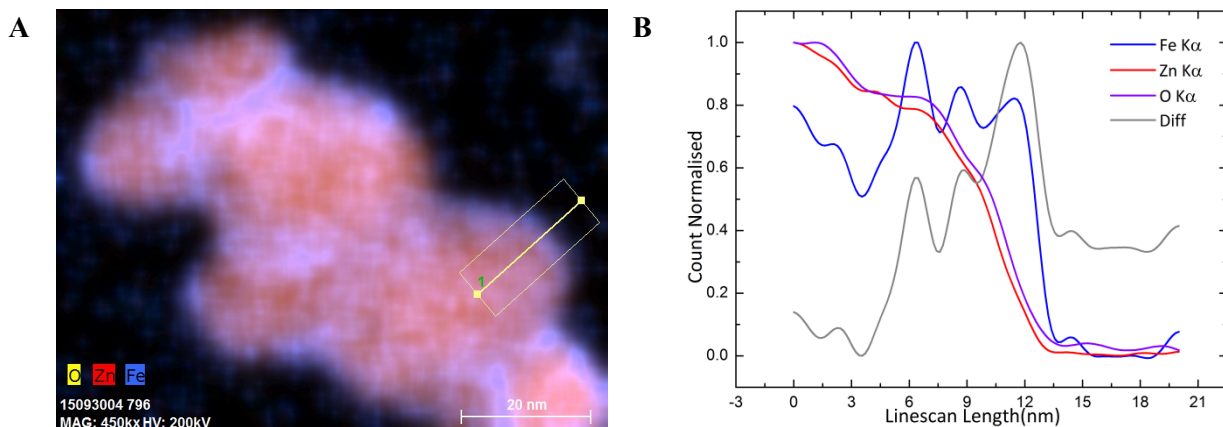
Figure 4: (a) TEM-EDX showing Fe, Zn and O intensity (b) Normalized Intensity along the yellow line

A difference plot between Fe and Zn counts (Fig. 4b) peaks near the surface region indicates an iron oxide coating and the core-shell nature of the sample. Individual area scan from core and shell region (Fig. 3d- Area 1&2) also show the similar interface behavior. Area scan data depicts higher count for Fe in the shell relative to the core, whereas Zn intensity remains constant throughout the core and falls intensely in the shell.

EDS data in Fig. 5 show the identification of the Zn, Fe, and O_2 atoms in the oxidized CSNPs (sample 1). Quantitative information deduced from the EDS calibration are provided in tbl. 1 shows the Fe phase percentage as low as 2.17%. This suggests the ultra-thin coating of 0.5- 2nm found in the TEM. Further reduction inside the tube furnace produces two reduced sample used in structural-property comparison throughout the article. The reduced sample has been prepared at an annealing temperature of 500K at N_2-H_2 or Ar-H_2 ambient applying just over the atmospheric pressure. Tbl. 3 shows the increase of Fe phase percentage to 12.19% for sample 2. TEM suggests the presence of stand alone iron oxide nanoparticulate in sample 2. Sample S2 has been used for the luminescent comparison only.
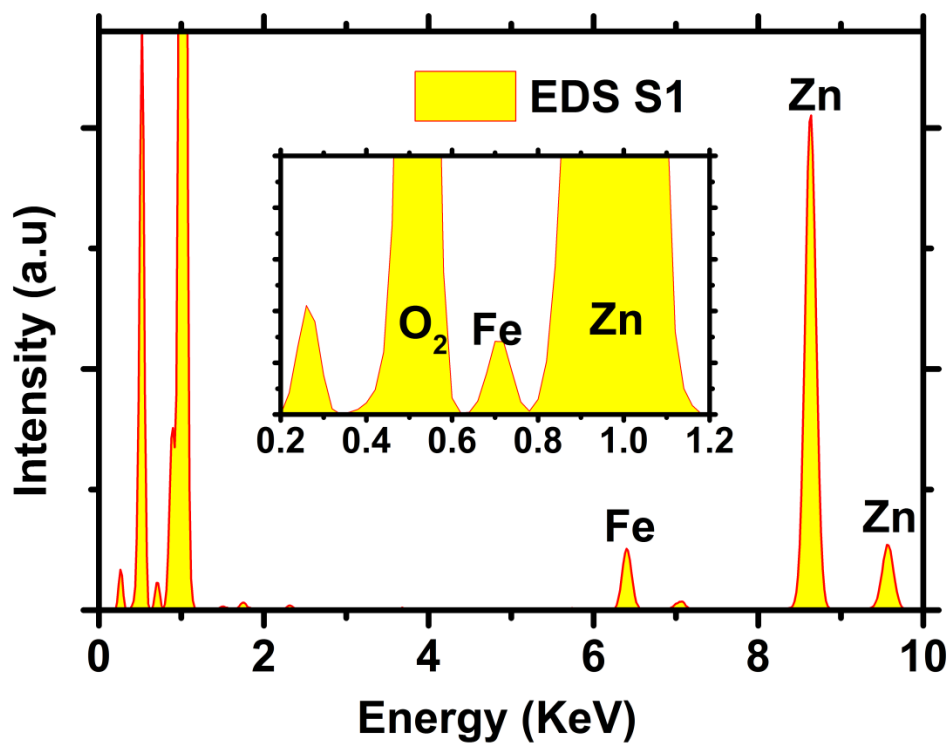
Figure 5: Background and C peak subtracted EDS spectrum of sample 1 showing the intensities from Zn, Fe and O_2 atoms.

Table 1: EDS quantitate analysis results from sample 1

Element	Excitation	Weight %	Atomic %
O	K-Line	24.90	57.36
Fe	K-Line	3.30	2.17
Zn	K-Line	71.80	40.47

Table 2: EDS quantitate analysis results from sample 2

Element	Excitation	Weight %	Atomic %
O	K-Line	20.27	50.00
Fe	K-Line	18.10	12.79
Zn	K-Line	61.63	37.21

Table 3: Diffraction results of the ZnO NP and oxidized CSNP

NP(ZnO)				Oxidized CSNP(ZnO)			
2θ	hkl	d(Å)	Area	2θ	hkl	d(Å)	Area
31.7809	010	2.81337	1200.497	31.78480	010	2.81303	754.714
34.4219	002	2.60332	915.285	34.44590	002	2.60156	627.712
36.26472	011	2.47515	2951.008	36.27393	011	2.47454	1772.855
47.54851	012	1.91077	1034.495	47.56968	012	1.90997	700.896
56.61893	110	1.6243	2503.752	56.62631	110	1.62411	1573.866
62.86507	013	1.4771	3045.682	62.90168	013	1.47633	1828.268
66.40475	020	1.40669	479.854	66.41371	020	1.40652	301.626
67.96936	112	1.37806	2512.344	67.99065	112	1.37768	1683.543
69.11475	021	1.358	1483.267	69.12717	021	1.35778	904.242
72.56702	004	1.30166	259.899	72.62391	004	1.30078	158.139
76.98709	022	1.23757	501.002	77.00945	022	1.23727	334.914

Diffraction peaks of ZnO NPs from the planar indices (010), (002), (011), (012), (110), (013), (020), (112), (021), (004), and (022) agree with the wurtzite structure (ICSD) with a lattice parameter of a = 3.2486 Å and c = 5.2066 Å (tbl. 3). Comparison between NPs and CSNPs (oxidized) lattice parameters (tbl. 3) reveals that the ZnO structure does not change much after annealing. Similar peak position, area (relative), and planar distance indicate that ZnO NPs remains in the same wurtzite phase during oxidation. Rietveld analysis of the reduced CSNPs gives the similar structural information. Little change in the lattice constant (oxidized-3.2512 Å & 5.20854 Å, reduced 3.2451 Å & 5.1985 Å) can be addressed to the residual strain (annealing) and surface interaction of the ZnO NPs. Rietveld analysis

assumes a crystal size of 20 nm (from Fig. 2). Calculated XRD powered pattern of magnetite (Fe_3O_4) and γ -Fe_2O_3 using Mercury 2.0 shows 2theta angle variation as low as 0.35 degree in specific planes (Fig. 6b). The lattice constants for Fe_3O_4 and γ-Fe_2O_3 are almost similar. There is no straightforward technique to identify between the Fe_3O_4 and γ-Fe_2O_3 from the XRD data. Due to the zero error, instrument error, low phase percentage, and solid-state assumption for nanomaterials in Rietveld refinement, it is a challenge to detect materials structural phase between Fe_3O_4 and γ-Fe_2O_3 with conviction.

The iron oxide diffraction peaks corresponding to the Miller indices value (hkl) of (022), (311), (004), (422), (333), (511), (044), (062), (533), and (444) are present both in reduced and oxidized CSNPs (tbl. 4). Peak positions (2θ), planar distances, and areas(relative) of the peaks are identical. This implies shell phase (SP) is either Fe_3O_4 or γ-Fe_2O_3. However, visually distinct color rules out the possibility of the reduced and oxidized SP being the same. For a coating of less than 3nm, the γ-Fe_2O_3 phase is thermodynamically more favorable than Fe_3O_4(Birkner and Navrotsky, 2017). This is since iron defect lowers surface energy. As γ-Fe_2O_3 is a relatively oxidized defect structure of Fe_3O_4, it is safe to assume that we reduced the γ-Fe_2O_3 structure to Fe_3O_4.So the assumption is annealing in the presence of Ar-H_2/N_2-H_2ambient reduces γ-Fe_2O_3 to Fe_3O_4. Following this assumption, oxidized and reduced CSNPs have been fitted with γ-Fe_2O_3 and Fe_3O_4 crystallographic information file (CIF). The lattice constant of the γ-Fe_2O_3 and Fe_3O_4 in the oxidized and reduced CSNP measured from the Rietveld refinement is 8.4609 Å and 8.4098 Å, respectively.

Table 4: Diffraction results of the maghemite and magnetite phase from the oxidized and reduced CSNPs

Oxidized CSNP(Maghemite)				Reduced CSNP(Magnetite)			
2θ	hkl	d(Å)	Area	2θ	hkl	d(Å)	Area
29.90385	022	2.98555	45.954	30.02974	022	2.97332	17.483
35.22066	311	2.54609	176.942	35.3703	311	2.53566	55.451
42.80028	004	2.1111	58.931	42.98505	004	2.10246	13.291
53.08785	422	1.72371	55.538	53.32342	422	1.71665	21.483
56.58746	333	1.62513	35.61	56.84132	333	1.61847	10.015
56.58746	511	1.62513	106.831	56.84132	511	1.61847	42.187
62.13091	044	1.49278	283.962	62.41505	044	1.48666	91.093
70.46903	062	1.33518	36.016	70.80228	062	1.32971	14.517
73.47761	533	1.28776	69.574	73.82983	533	1.28249	24.963
78.39406	444	1.21885	21.897	78.77895	444	1.21385	5.318

Fig. 6a outlines a good agreement between the experimental and Rietveld deconvoluted data of the oxidized CSNPs. Glass background has been subtracted from the data before fitting. Rietveld refinement in TOPAS confirms the presence of the wurtzite ZnO and inverse spinal γ-Fe_2O_3 phase. For iron chloride and zinc oxide initial weight ratio from 1:2 to 1:50, Rietveld quantitative analysis show 1.3 to 8.4% presence of the γ-Fe_2O_3 phase. All data, Figure, and table presented in this paper correspond to sample S1 (1:2 initial mixture ratio of ZnO and $FeCl_3.6H_2O$) unless otherwise specified. The black circle in Fig. 6a links to the intensity from the γ-Fe_2O_3 structure. Fig. 6a (i, ii) illustrates an excellent fit of the γ-Fe_2O_3 CIF (ICSD). The goodness of the fit (GOF), Rexp, Rwp, and Rp for the oxidized CSNPs are 5.96, 1.22, 7.29, and 5.23, respectively. Atomic positions of Zn (x=1/3, y=2/3, and z=0) and
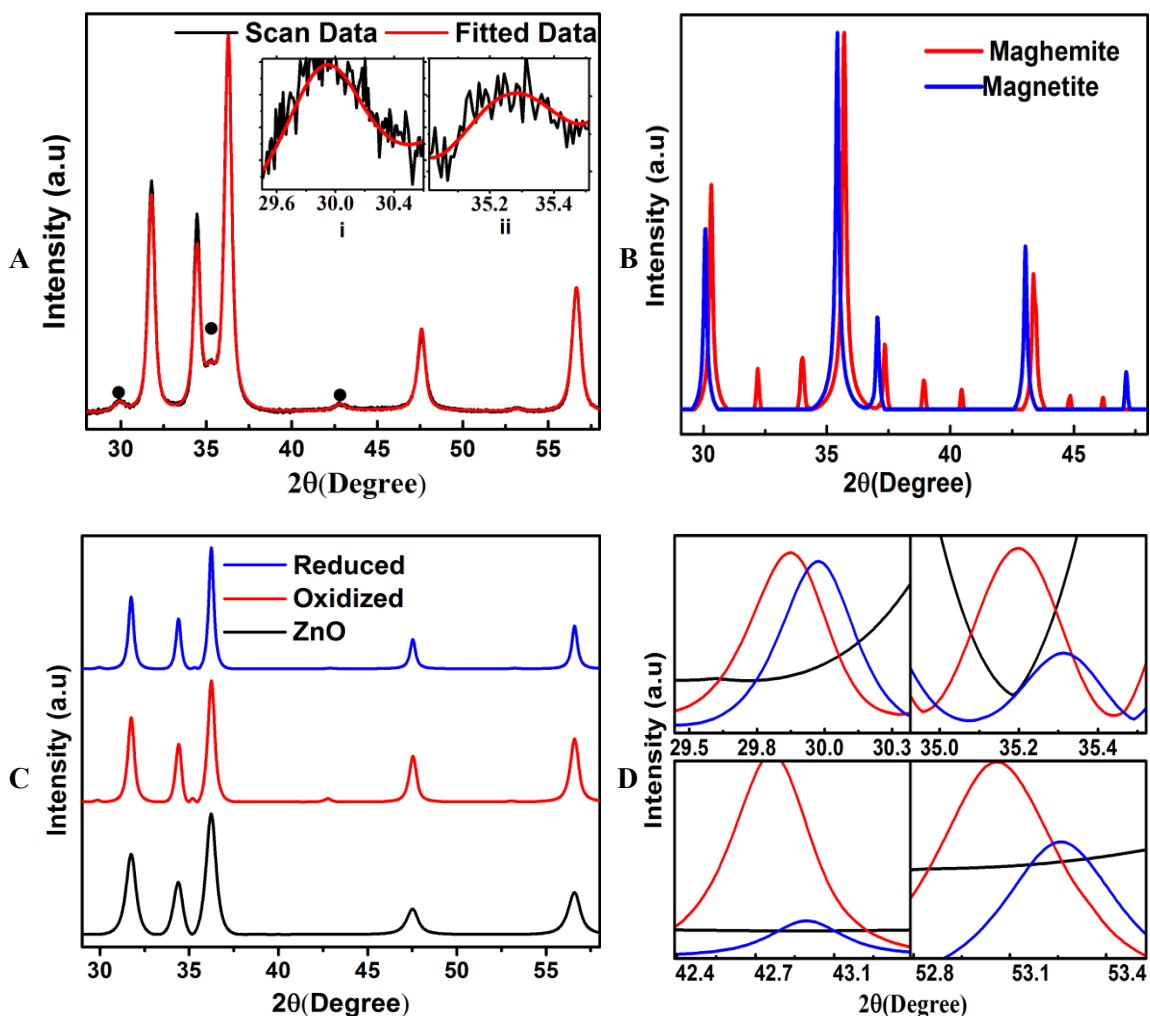
Figure 6: X-ray Diffraction of the (a) Experimental and refined data of the oxidized CSNP (b) γ-Fe$_2$O$_3$ and Fe$_3$O$_4$ from the Crystallographic Information File (c) Reduced CSNP, Oxidized CSNP, and ZnO NP (d) showing the γ-Fe$_2$O$_3$ and Fe$_3$O$_4$ Peaks (Reproduced from the data of the Fig. 6c)

Fe$_2$O$_3$(x=1/3, y=2/3, and z=3/8) were constant throughout the refinement. Atomic positions for the Fe and Fe$_2$O$_3$ ions are given (tbl. 3). Occupation and temperature dependent parameter were not changed during the refinement. 11 identified ZnO peaks (tbl. 2) in the refinement are present on the XRD pattern of the oxidized CSNPs (Fig. 6a, 5c). Fig. 6c display the XRD pattern of the ZnO NPs, oxidized and reduced CSNPs. The bottom black pattern corresponds to the ZnO NPs XRD. The GOF for the refinement is 2.69. R values (Rexp=1.46, Rwp=3.92,

and Rp=3.04) for the refinement is acceptable. Rietveld refinement in Topas (Fig. 6c, 5d) shows the similarity of the SP XRD pattern in the Ar-H_2 or the N_2-H_2 environment. No impurity phases of FeO, Fe_2N, Fe_3N or any other compound was found during the refinement. Four significant iron oxide peaks in Fig. 6d (reproduced from Fig. 6c) shows the similarity and presence of the γ-Fe_2O_3 and Fe_3O_4 atomic structure from the oxidized and reduced CSNP correspondingly. This indicated that the fitting value of the reduced and oxidized structure is almost similar. Atomic x, y, and z position of the structural refinement of the γ-Fe_2O_3 and Fe_3O_4 are specified in tbl. 5 and 6 separately.

Table 5: Atomic positions of the maghemite

Site	x	y	z	Atom
Fe-oct	0.5	0.5	0.5	Fe+3
Fe-tet	0.125	0.125	0.125	Fe+3
O	0.25	0.25	0.25	O-2

Table 6: Atomic positions of the magnetite

Site	x	y	z	Atom
Fe2+	0.724	0.3757	0.25	Fe+2
Fe3+	0.246	0.1107	0.0879	Fe+3
O1	0.506	0.25	0	O-2
Fe_2O_3	0.18	0.2447	0.25	O-2
O3	0.296	0.4899	0.098	O-2

It is possible to deconvolute the peaks and identify the phases by constructing a calibration curve from the ideal nanopowders XRD(Kim et al., 2012). However, a convenient approach is drawing the conclusion through complementary techniques as SQUID measurement. The successful detection of the shell atomic structure is likely by combining the XRD results with SQUID data and crystallographic parameters. Since solid state refinement techniques like Rietveld cannot produce highly accurate values for nanomaterials having dimension lower than 5 nm, the shell thickness can be more accurately modeled and measured using software package DIFFEV which uses Debye formula (Niederdraenk et al., 2006).

Magnetite and Maghemite are two of the three naturally prevalent iron oxides. They are magnetic oxides of maximum importance. Low octahedral occupancy energies are the reason of their inverse spinel structure. Oxygen ions occupy closed packed assembly. Fe (II) ionic state is not present in Maghemite. Fe(III) ions shares both octahedral and tetrahedral sites. Cation vacancies in octahedral site preserve the charge balance. In Magnetite, Fe(II) ion remains in octahedral sites. Fe (III) sit both in tetrahedral and octahedral sites.

Four and five d orbital unpaired electron in complex inverse spinel structure causes strong magnetic behavior. Magnetite is the strongest ferromagnet among all the TMOs. Maghemite is ferrimagnetic at room temperature. Curie temperature for the Magnetite is 850 K. Maghemite is a metastable material and loses susceptibility with time. This makes determining the Curie temperature of maghemite difficult. Bulk Maghemite Curie temperature is reported to be in between 820-986 K (Teja and Koh, 2009). Having the dimension lower than 20nm scale in at least one dimension causes both Magnetite and Maghemite to behave like a single domain material. Superparamagnetic behavior dominates in the NPs length scale and surface spin contribution causes magnetic anisotropy. This causes the Curie temperature

to drop (Blaney, 2007). Less than 1µm maghemite nanospheres non-collinear spin contribution at or near the surface causes magnetic anisotropy and is no longer negligible. Sub-micron size Maghemite NPs are composed of fine crystallites(Morrish and Haneda, 1980).

Fig. 7 outlines the temperature dependent FC-ZFC magnetization of oxidized and reduced CSNPs. Oxidized CSNPs FC-ZFC show the Curie temperature as low as 15K. Such drastic lowering of the Maghemite Curie temperature may be due to the ultra-thin coating (0.5-3 nm), surface magnetic anisotropy, and interaction with the ZnO interface. Fig. 7 indicates the above 300K Curie temperature for the reduced sample either in N_2-H_2 or Ar-H_2 ambient. Ferromagnet can retain the magnetic response in the nanoscale more than the ferrimagnets.

Magnetization curve shows the change of the magnetic hysteresis of the annealed samples. Reducing the sample increases the coercivity and remnant saturation. Ar-H_2 reduced sample shows a higher value of the remnant and saturation magnetization than the N_2-H_2. Ar-H_2 reduced CSNPs show a higher value of the coercive field than the N_2-H_2 reduced sample at 5K. Magnetization curve shows the change of the magnetic hysteresis of the annealed samples. Reducing the sample increases the coercivity and remnant saturation.

Ar-H_2 reduced sample shows a higher value of the remnant and saturation magnetization than the N_2-H_2. However, the Ar-H_2 reduced sample shows a lower value of the coercive field than the Ar-H_2 annealed CSNPs and retains the near superparamagnetic behavior wonderfully. Magnetic moment (emu/gm) of the CSNPs is far low. This is understandable considering iron oxide comprises less than 5 weight percent of the CSNPs. Fig. 7, 8, and tbl. 5 show the successful change in the magnetic parameter (coercive field,
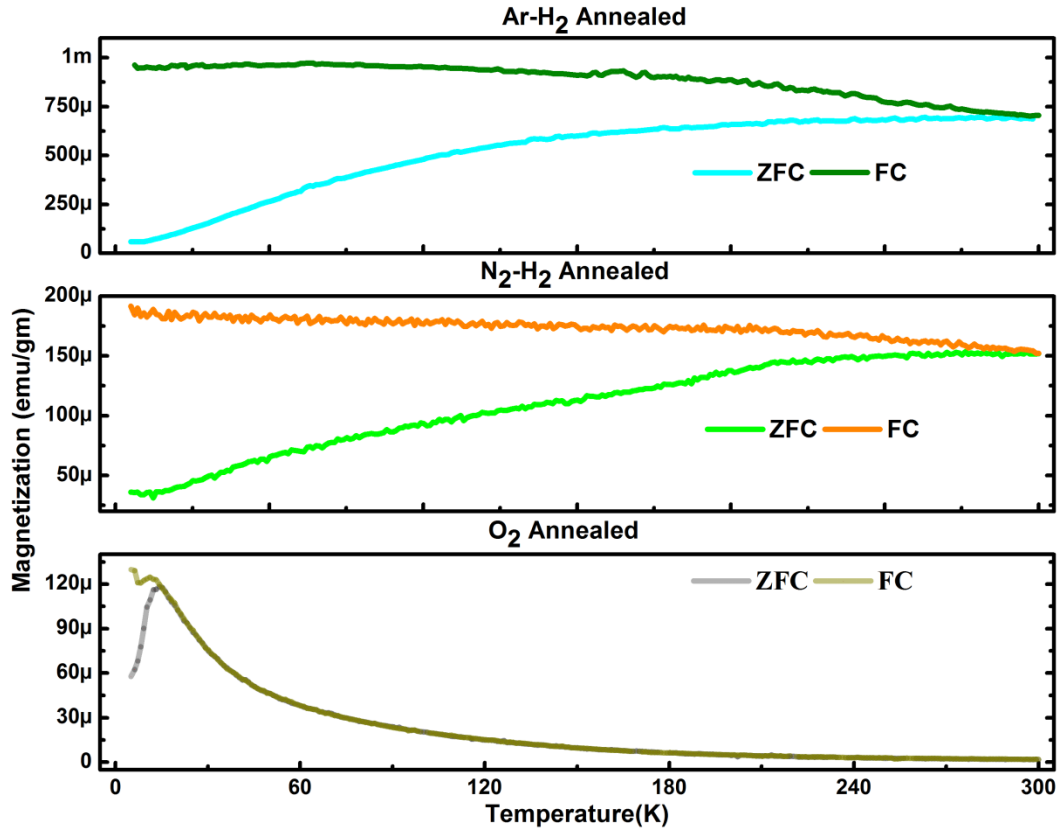
Figure 7: Temperature Dependent ZFC and FC Magnetization (FCW)

remnant and saturation magnetization) of the CSNPs. This implies that the CSNPs are tunable

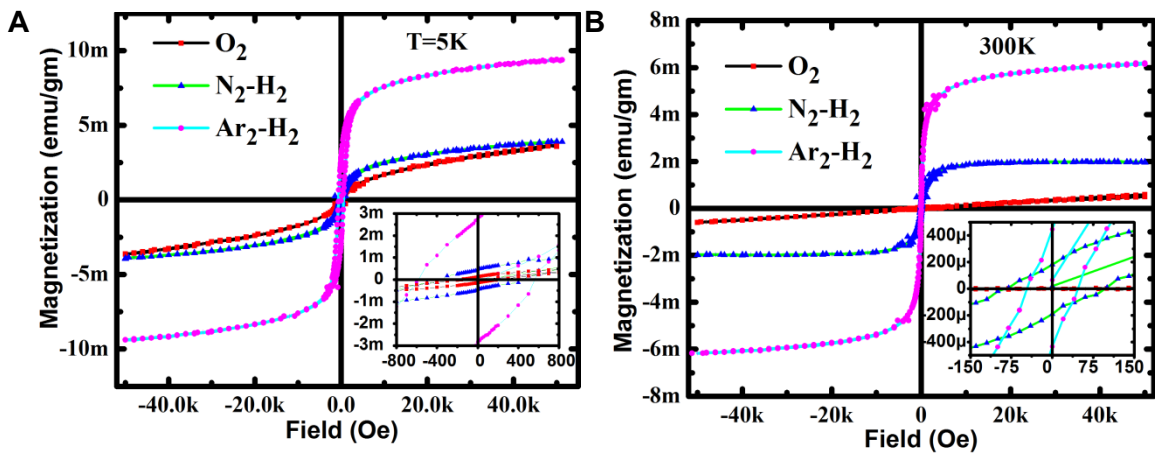for soft(superparamagnetic) and hard (ferromagnetic) applications.

Figure 8: Magnetization curve of S1 O_2, N_2-H_2, and Ar-H_2 annealing (A) 5 K hysteresis (B) 300 K hysteresis

Table 7: Hysteresis Parameters of the oxidized and reduced CSNPs

Annealing Environment	Temperature	Coercive Field (Oe)	Remnant Magnetization (emu/gm)	Saturation Magnetization (emu/gm)
O2	5K	220	100×10-6	600×10-6
O2	300K	0	0	--
N2+H2	5K	420	500×10-6	4.2×10-3
N2+H2	300K	100	200×10-6	1.3×10-3
Ar+H2	5K	580	3000×10-6	10×10-3
Ar+H2	300K	50	470×10-6	6×10-3

Strong excitonic and defect ZnO luminescence depend on doping, synthesis parameters, crystallography, size, shape, temperature, and surface properties. Intrinsic defects emission spans the entire visible spectrum from blue to red. In theory, the presence of more than 10 intrinsic defect makes ZnO as an n-type luminescent semiconductor. Fig. 9 shows the intensity of the UV and visible emission of ZnO NPs with an excitonic wavelength of 325 nm. Deconvoluted peak 1 and 6 corresponds to the excitonic emission, whereas peak 2, 3, 4, 5, and 7 comes from the deep level emission (DLE) ranging 400 to 750 nm. Peak 1 corresponds to the band edge emission of ZnO. Quantum size effect increases (peak 6) the ZnO energy gap (Talam et al., 2012). DLE of ZnO is a superposition of many defects emission. ZnO NP DLE primarily corresponds to the Zni, Oi, Vzn, VZn-, Vo, Vo+, OZn(Liu et al., 2010). Wide DLE means wider distribution (Fig. 2) of the nanoparticle size and shapes(Talam et al., 2012). Since the last decade, no consensus has been achieved on the principle intrinsic defect state responsible for ZnO luminescence.
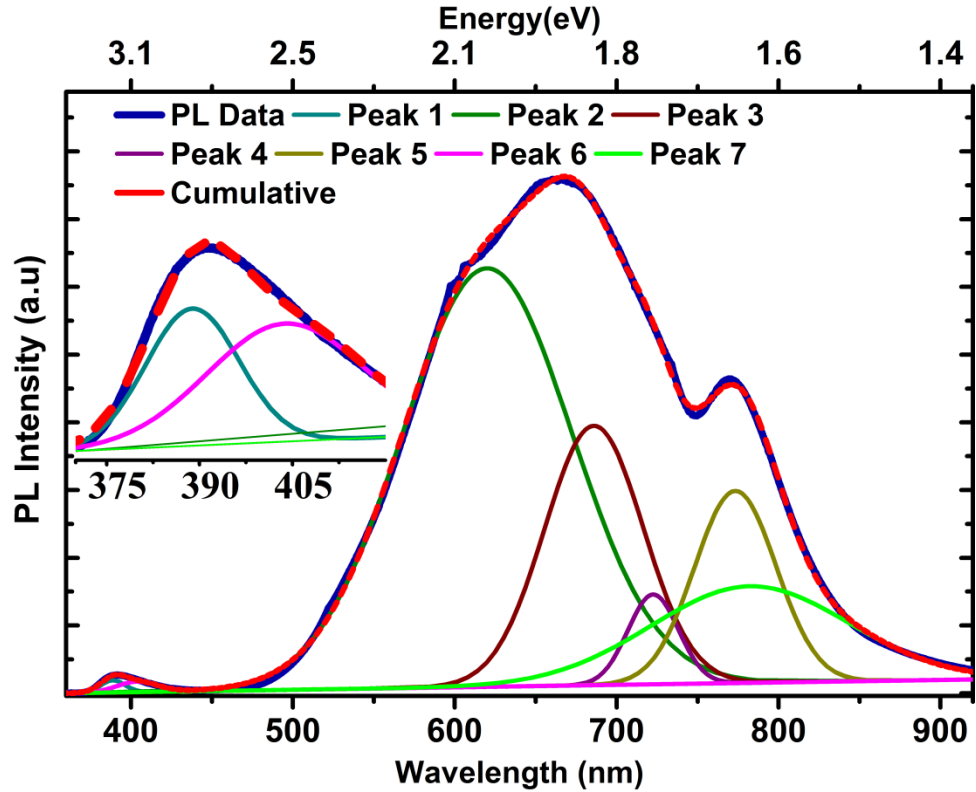
Figure 9: Photoluminescence of ZnO NPs

Fig. 10 shows the different defect state energy from multiple sources. Size, shape, and synthesis parameter can easily change the structural and luminescent properties of ZnO. Lowering the size increase the structural and surface defects which consequently causes a strong DLE (Rodnyi and Khodyuk, 2011).

Broad emission around 2.45 eV (Fig. 9, near peak 2) has been identified for oxygen vacancy sites(Leiter et al., 2003). This is also supported by a synthesis of CSNPs in N_2 and O_2 ambient(Rodnyi and Khodyuk, 2011). One literature point out the V_{zn} as the primary source of 2.45 eV emission(Reynolds et al., 1997; Willander et al., 2010).

Figure 10: Blue and Green Band Emission of ZnO NPs from numerous sources (adapted from Vempati et. al., Nanoscale Research Letters 20127:470)

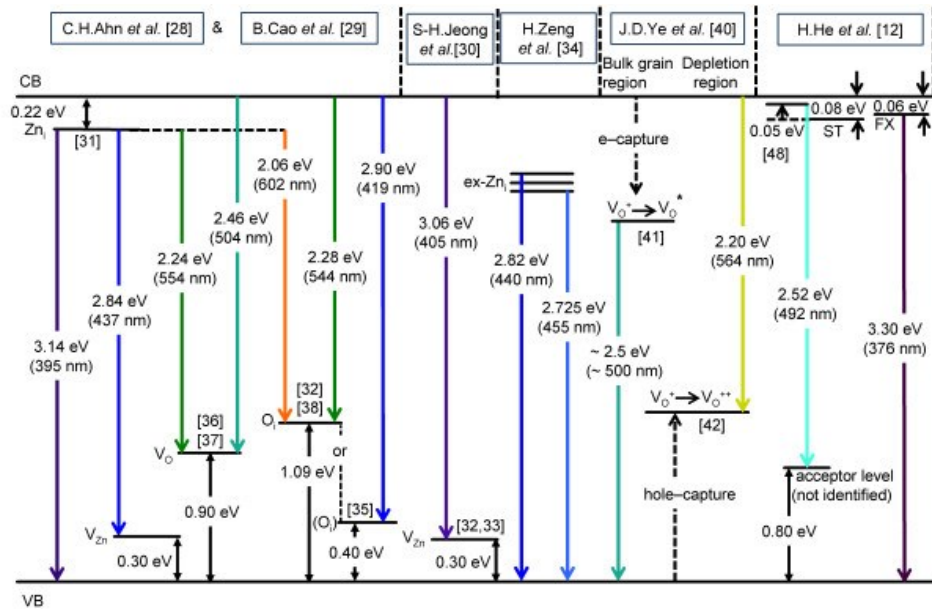First principle calculation show O_i and V_{zn} intrinsic defects dominate in oxygen rich ZnO material(Janotti and Van De Walle, 2007).V_o and Zn_i sites were presumed as dominant in zinc rich synthesis environment. This claim later proved to be incorrect(Janotti and Van De Walle, 2007). Indirect recombination of the excited electrons and holes may be responsible for the green emission centered at 570 nm(Thandavan et al., 2015). $V_O Zn_i$ cluster is identified for ZnO nanostructure around 2.16 eV (peak 2, Fig. 9) below the conduction band minimum(Willander et al., 2010). Octahedral site occupancy of O_i creates a deep acceptor transition in 0.72 and 1.59 eV(Janotti and Van De Walle, 2007). Peak 5 and 6 show the doublet band emission of ZnO. Significant contribution in the doublet emission may originate from the surface defects, inter defect states transition and nearly free exciton recombination. O_{zn} defect acts a deep level acceptor and contributes to the emission at 1.52 and 1.77 eV(Willander et al., 2010). Surface oxygen or surface hydroxyl groups produce red emission (peak 3 and 4 in Fig. 9) (Vempati et al., 2012).

30

Fig. 11 compares the defect emission of the ZnO NP and oxidized s1 and s2 CSNPs. S1 and s2 sample contains DLE spectra are normalized through the excitonic emission near 390 nm. CSNPs defect intensity decreases with increasing shell thickness. A higher amount of maghemite (S2) SP red shifts the excitonic emission by 5 nm (Fig. 11). Interaction in the ZnO/iron oxide interface modify the surface defects. Hydroxyl group on the ZnO NPs surface interacts with iron oxide. This can passivate the defect states to decrease or increase the defect contribution from the surface. Since the defect peak is too broad, it is a challenge to address the source of the defect peak reduction. Considering the nano-size and larger surface area of the NPs, surface modification may be a prime reason. The broadness of the peak makes it difficult to attribute the reduction to one or two peaks with authority. Absorption by the incoming and emitted photons by the coating is a possibility since the DLE remains identical and resultant peak reduces.

The Raman spectra have been collected with a green excitation wavelength of 513.4 nm. Raman measurements respond to the subtle change in the crystallinity, doping. line and point defects, and surface disorders (Silambarasan et al., 2015). Vibrational modes are a signature of materials molecular structure. Fig. 12 shows the normalized and background subtracted vibrational modes of NPs and oxidized CSNPs. Peaks around 327-333 nm, 435-438 nm, and 574-584 nm correspond to the $E_2^H - E_2^L$, E_2^H, and $A_1(LO)$ modes of the ZnO NPs(Silambarasan et al., 2015). Oxygen vacancies contribute to the enhancement of the 580 nm Raman band of the CSNPs (Camarda et al., 2016). Oxygen vacancy site may decrease through oxidation at 500^0C as well as iron oxide interface interaction. Bulk ZnO material does not display $A_1(LO)$ mode. The significant intensity of the $A_1(LO)$ peak features the nano size of the material (Camarda et al., 2016).Reduction of E_2^H vibrational mode intensity implies the
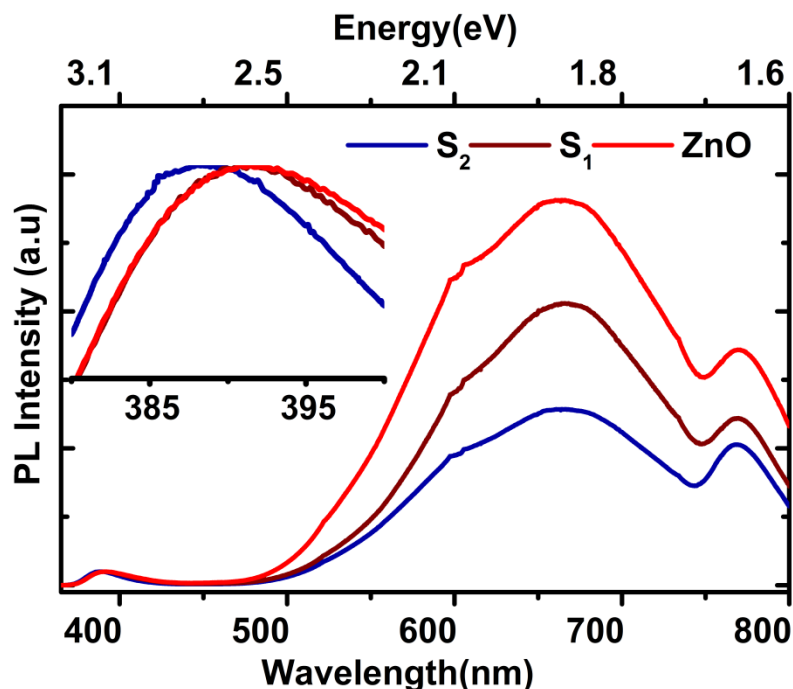
Figure 11: PL comparison between ZnO NPs and oxidized CSNPs (s1 and s2)

the possibility of Fe doping or bonding near the ZnO NP surface. The breaking of the wurtzite

transitional symmetry by iron causes the drop of this peak. (Silambarasan et al., 2015).

Defect states at 675 nm in the CSNPs are either from the ZnO intrinsic defect or

inverse spinel iron oxide (Sato-Berrú et al., 2007). No consensus has been reached so far as

the source of the 675 nm mode. The similar hypothesis seems can explain the intensity

increase of the peak around 396 nm. 500 nm ZnO NPs Raman peak (Not visually evident on

the Fig. 12) associated with E_1(TO) and E_2^L mode (Silambarasan et al., 2015) gets reduced in

the CSNPs. This may be due to the internal stress and strain on the wurtzite caused by

annealing. Similar phenomena occur for the peak around 396 nm. XPS data give quantitative

and chemical information of the surface. Though signals reasonably contribute till the 10-nm

depth of the sample, it is widely known that top 5 nm of the sample generates 80% of the

photoelectron counts. From the surface to the10 nm depth, XPS analysis is nonlinear.
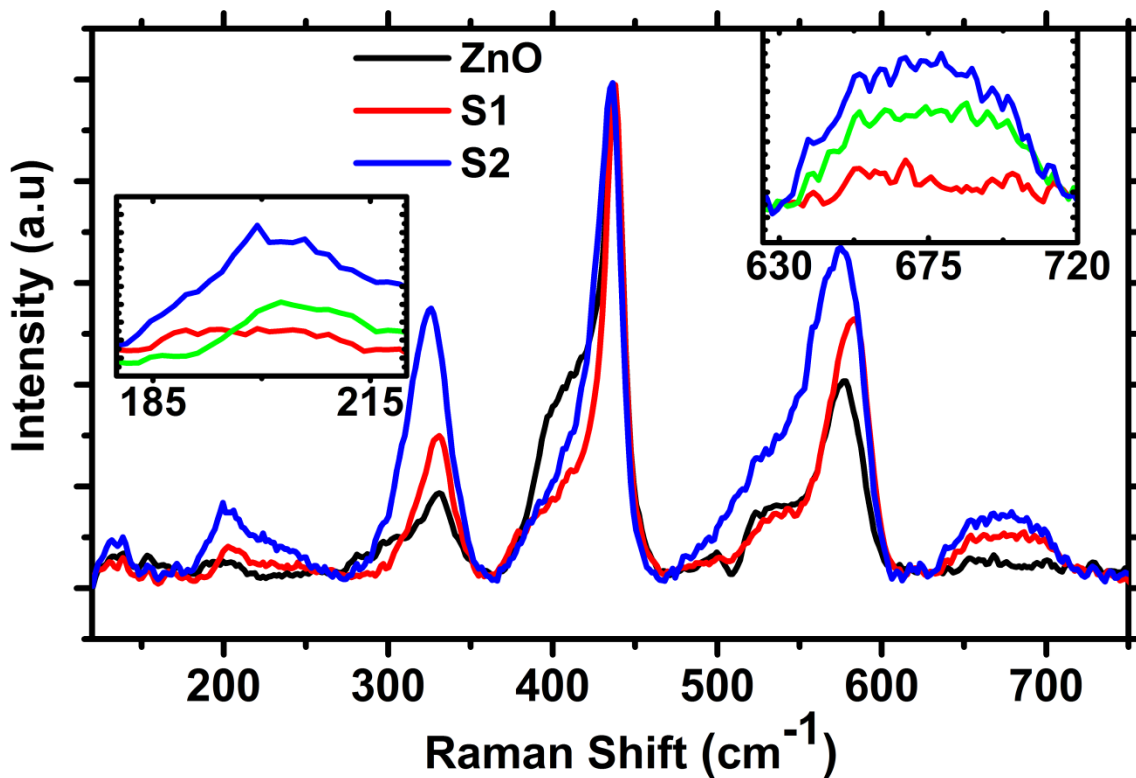
Figure 12: Comparison of the vibrational modes of ZnO NPs and oxidized CSNPs

Survey scan of the oxidized CSNPs at Fig. 13 shows the presence of Fe 2p, Zn 2p, and O$_2$ 1s XPS peaks. Surface charging was minimized during the data acquisition. No impurity phase other than carbon has been found in the survey scan. Carbon C 1s peak has used to calibrate the scan. Quantitative analysis of the XPS data has been done using CASA software. Satellite peaks of iron were not included during the analysis. Individual value of the orbital RSF was used during the quantization. Fe Shirley background was added using skip CASA XPS feature to make sure that no background cuts through the data. Fe Auger peaks were not used during the quantitative analysis of the data. This ensures that the atomic iron percentage in the sample is not overestimated (Biesinger et al., 2010). Results of the quantitative analysis of the oxidized CSNPs CASA XPS in tbl. 8 show an increase of iron atoms percentage than
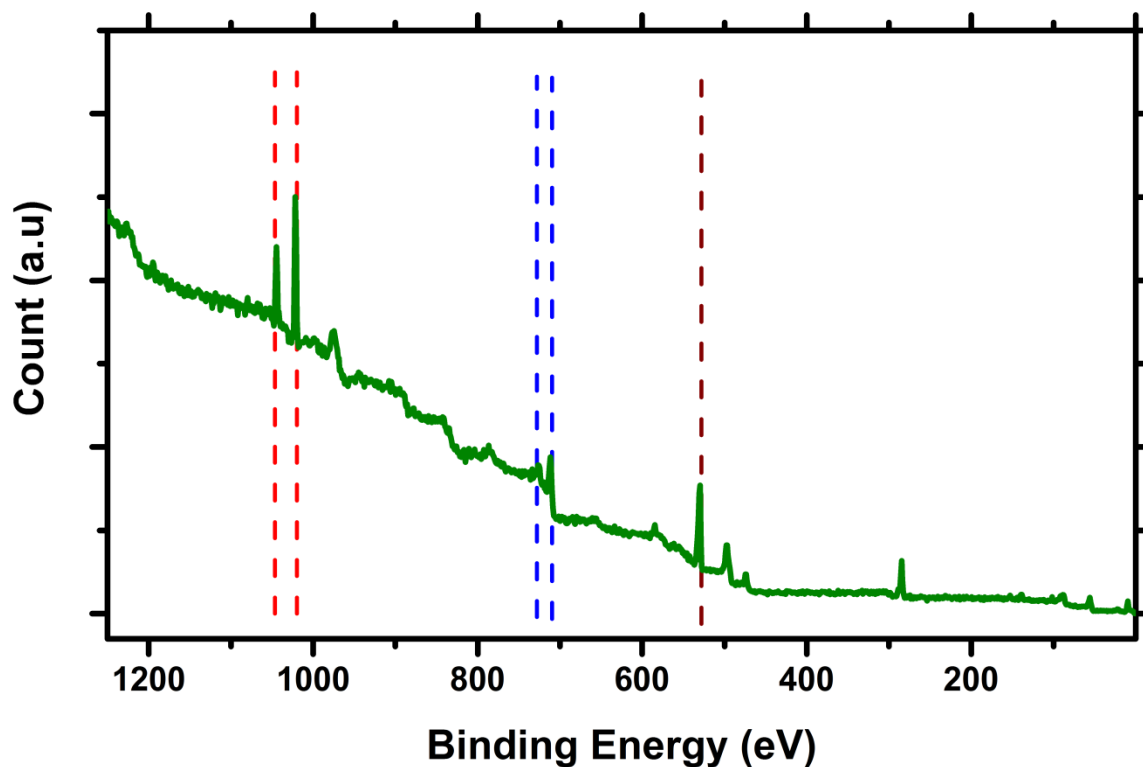
Figure 13: XPS survey scan of oxidized CSNPs (s1)

the previously determined with EDS. This is expected considering only a few nm surface layers is contributing to the spectra. Higher phase percentage of the O 1s peak indicates a higher stoichiometric ratio between the O_2 and Fe atom. Which implies there is a higher possibility the surface layer would be maghemite than magnetite. Zn phase percentage has been significantly reduced compared to the XRD and EDS phase quantization.

Table 8: Analytical results from oxidized CSNPS (S1)

Element Peak	Position	Atomic %
O 1s	529.1	66.68
Fe 2p	710.71	12.03
Zn 2p	1021.71	21.3

A high resolution (HR) scan of the Fe 2p peak in Fig. 14 reveals the presence of Fe 2p3/2, Fe 2p1/2, and their satellites. The spectra of the 2p3/2, 2p 3/2 satellite, 2p 1/2 and 2p 1/2 satellite of Fe along the 710.7, 719.6, 725.1, and 733.4 nm line show the similarity with the results of M.C. Biesinger et al. / *Applied Surface Science 257 (2011) 2717–2730* of Fe (III) state. No peak around 706 nm rules out the possibility of metallic iron in the sample. No satellites around 715 and 728 nm displays the absence of any Fe (II) atoms on the surface (Biesinger et al., 2010).
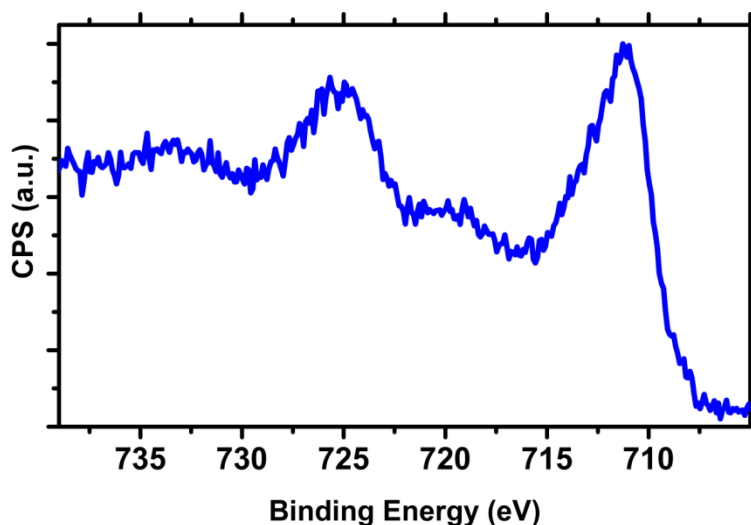
Figure 14: HR scan of Fe 2p orbitals of oxidized CSNPs (s1)

Fitting of more than one iron oxide phase is challenging due to background contribution and spectral overlaps. All analysis of iron oxide spectra inherently carries some error for a variety of reasons (Biesinger et al., 2010). Peaks have been fitted following the earlier works of Gupta and Sen in multiplet splitting for iron. All the peaks have been fitted using the line shape (CASA) Gaussian without any asymmetry. Deconvolution of Fe 2p ½ peak at Fig. 15 resembles with the Υ-Fe2O3. 2.4773 eV splitting between the $3e_g$(blue) and $2e_g$ (light pink) is close to the reported 2.5 eV value for maghemite(Klein et al., 1975). The
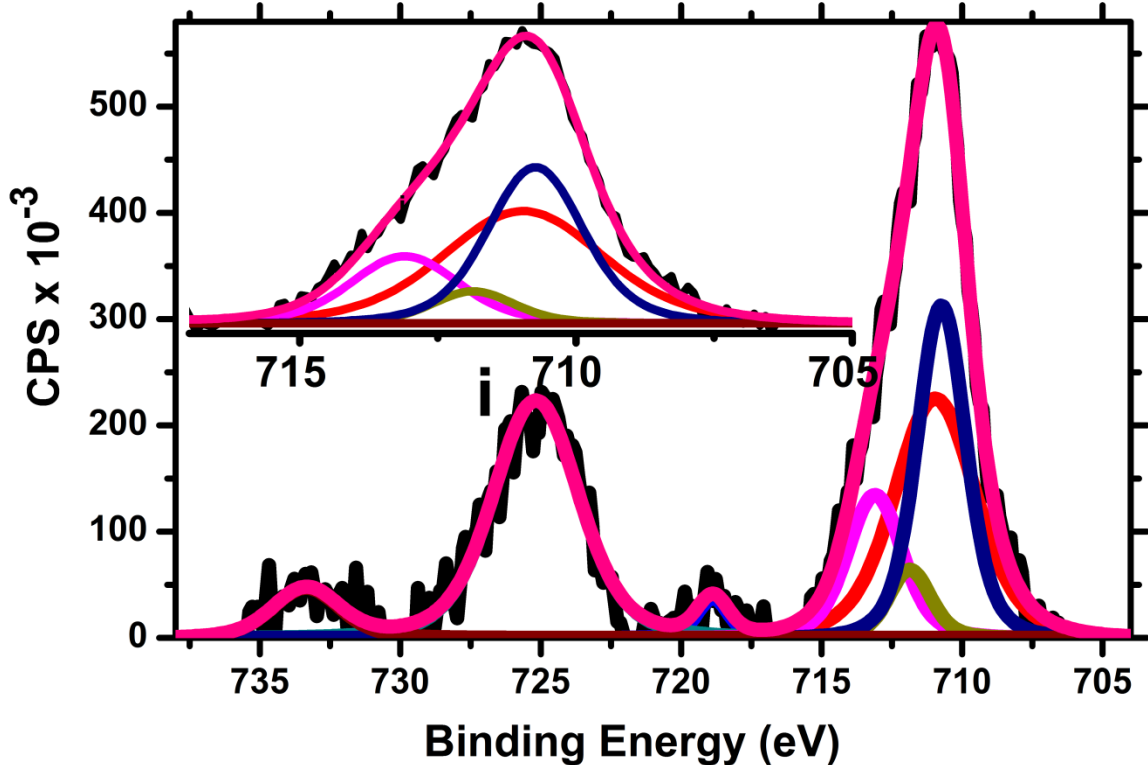
Figure 15: Deconvolution spectrum of the Shirley background subtracted XPS data

value of the all four deconvoluted peaks resembles with the high spin 2p3/2 structure of Υ -Fe2O3(Grosvenor et al., 2004). A Little shift in the absolute position can be attributed from not using the shake-up satellites and surface peak in the deconvolution. Deconvolution of the Fe 2p 3/2 peak conclusively proves the iron oxide phase to be magnetite.Reduction of the Zn counts in the CSNPs than the NPs also suggest a coating over the structure. Oxygen 1s HR scan data proves that there is no significant presence of the hydroxyl group on the surface.

Conclusion

The article proves the successful synthesis and modification of ZnO/Iron Oxide CSNPs in reasonable detail. Complex structure-property data have been analyzed by various

characterization methods. Reduction enables the magnetic tuning of the CSNPs through the

procedures described in the article. This may lead to the more efficient magnetic materials and

devices in future. Partial coating of the ZnO NPs with superparamagnetic iron oxide

(magnetite/maghemite) may open the door for new applications in biomedical.

ME BATIO₃-IRON OXIDE CSNP SYNTHESIS, CHARACTERIZATION, AND OPTIMIZATION

Abstract

Electrical and magnetic coupling is the key for electrical and magnetic cross-cutting devices. Ideal synthesis extracts the optimum property from the multifunctional materials. The article discusses the clean physio-chemical synthesis method of BatiO₃/iron oxide CSNPs. SEM and TEM show an excellent dispersion of nanoparticles. XPS confirms the maghemite phase in the oxidized CSNPs surface. The presence of the surface iron oxide in the CSNPs is adjustable through surface treatment and may change the coupling nature between the structures. XRD data confirm the crystallinity. Almost no iron oxide phase ensures there are no iron oxide particulates in the CSNPs.

Introduction

Magnetoelectric single-phase materials are very rare in nature. Rarity and the smaller value of the coupling parameters of the single-phase materials urge the necessity to design multi-phase magneto-electric materials. In nanoscale, all the properties are greatly dependent on size and shape. Dispersion and uniformity are the key feature of the synthesized nanoparticle to reproduce the property of interests. Sonochemical methods are growing interest for preparing unique nanostructured materials. On growing demand of the new set of nanomaterials for electronic, magnetic, biomedical devices make multifunctional multiferroics promising for the future nanotechnology. Growth in this field is depended on fabricating new compounds with strong multiferroic coupling. Multiferroic coupling in semiconductor devices promises to fill in few current limitation of the silicon industry.

Methods

A series of sonication and centrifugation process coats the BatiO3 NPs with the ions present in the FeCl$_3$ solution in DDI water. Commercially purchased BaTiO$_3$ NPs and FeCl$_3$.6H$_2$O were mixed in 1:2 weight ratio. A dip sonicator stirs the samples three times for 30 minutes each. Ions in the solution stick on the BaTiO$_3$ surface through physio-absorption. Annealing in oxygen atmospheric ambient changes the surface layer into maghemite. Diffraction pattern was observed by Cu k-α source and the state of the art LENXEYE XE detector. 513.6 nm laser excites sample at room temperature for the collection of vibrational modes. TEM data show the surface topography. The surface of the sample has been plasma etched before acquiring TEM data. TEM-EDS data collects the interface linescan to verify the core-shell nature of the NPs. XPS with an Al-Kα source has been carried out to inquire the chemical environment of the surface atoms. Surface charge in the XPS data has been neutralized using the flood gun. Fabrication and instrumentation of the BaTiO$_3$/ Iron Oxide CSNPs discussed in this article is completely reproducible in the experiment.

Results and Discussion

TEM data in Fig. 16 indicate the acceptable dispersion of the CSNPs. HAADF image in Fig. 16A shows the sample site used for EDS elemental mapping. Mapped only with the Ba atom count in Fig. 16B specifies a uniform distribution of the BaTiO$_3$ from the center to the surface of the NPs. Fig. 16C indicates an increase of the Fe atom count (intense color) near the surfaces/ interfaces. Linescan through the CSNPs interface shows an increase in Fe count. Ba and Ti count in the interface region are lowest among all the atoms. A slightly higher count for the oxygen in the interface region indicates the possibility of the iron oxide over BaTiO$_3$ NPs.
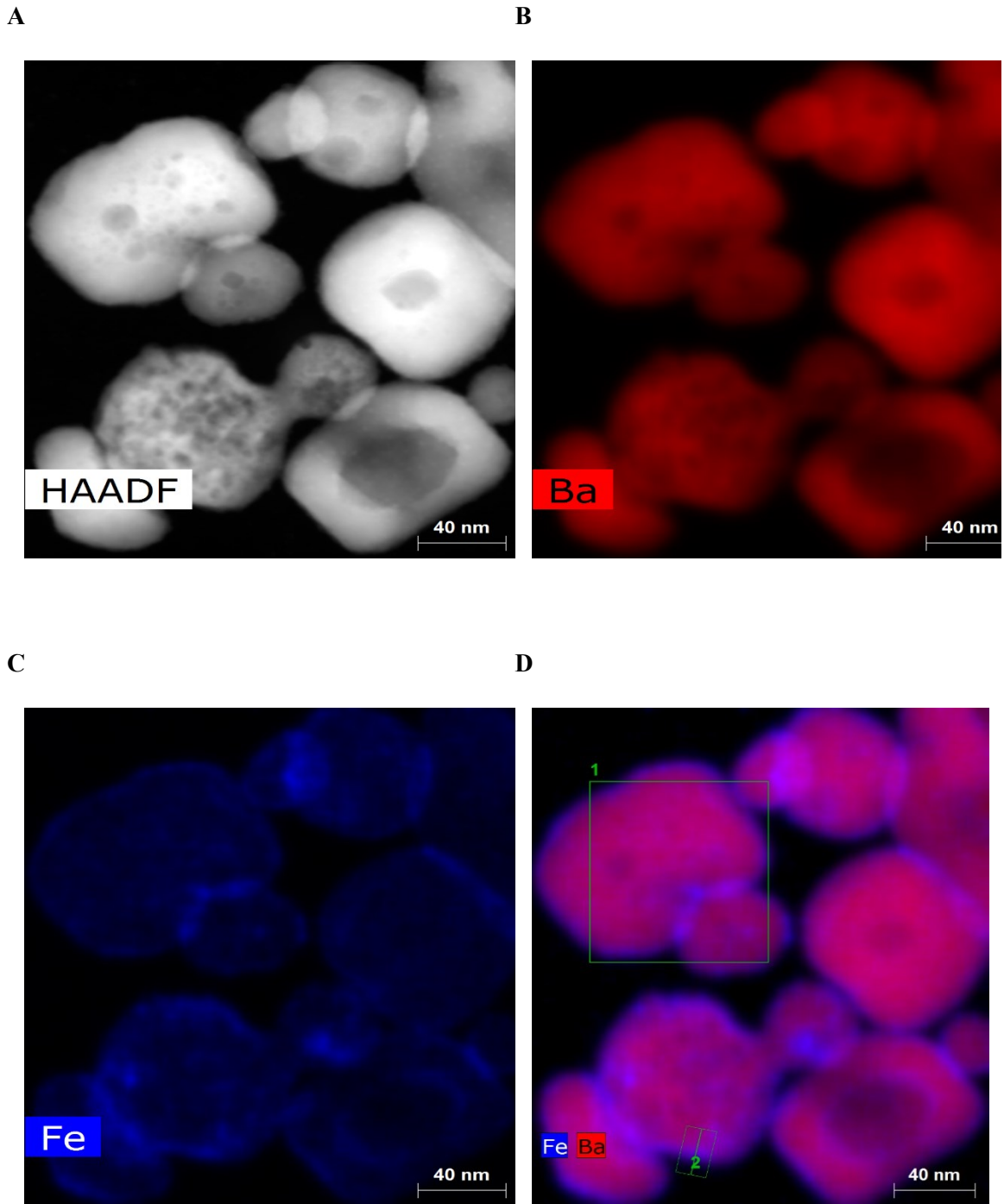
Figure 16: TEM colored mapping of the CSNPs (A) Sample region for HAADF imaging
(B) Intensity from the Ba atom (C) Intensity from the Fe atom
(D) Intensity from the Fe and Ba atom combined
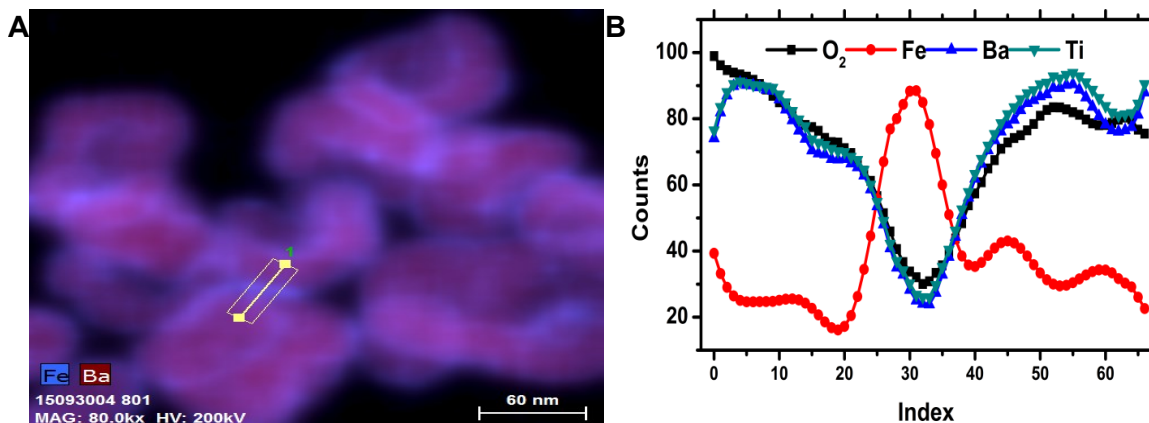
Figure 17: Linescan along the CSNPs interface (yellow line)

Diffraction peaks of the CSNPs show the presence of the crystalline $BaTiO_3$ structure (Fig. 18). No impurity phases have been found. Rietveld structure refinement using Topas gives a crystal size of 60.4 nm which is little higher than the commercial spec (50 nm) of the nanoparticles. $BaTiO_3$ Miller indices of (100), (110), (111), (002), (200), (201), (210), (211),

Figure 18: XRD diffraction data of oxidized CSNPs

(220), (221), (301), and (311) have been successfully identified in the oxidized nanoparticles. Increasing FeCl3.6H20 concentration in the initial mixture has almost no effect on their XRD. Both samples show similar phase percentage when fitted with $BaTiO_3$ and Υ-$Fe_2O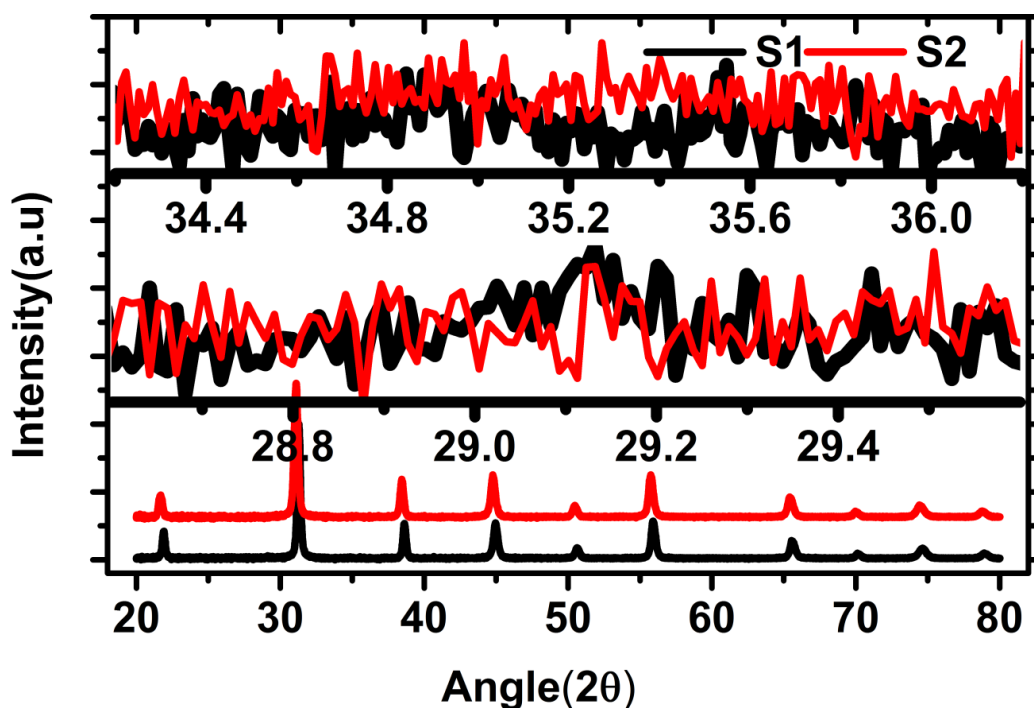_3$ phase. Zoomed in the picture around 29.15 nm and 35.2 nm in the Fig. indicates the possible presence of (220), and (311) plane of maghemite. The low intensity and higher FWHM from these two planes indicate a ultra-thin (few nanometers) coating in nanoscale.

XPS data confirms the presence of the Iron on the NPs surface (Fig. 19). Higher Fe count in the XPS data (3.05 %) than the EDS data (0.47 %) indicates the presence of Fe in the nanostructure surface. The lower quantitative presence of the Ba and Ti atoms from the CSNPs structure XPS data supports the core-shell nature of the synthesized nanostructures. All the relevant peaks in the CSNPs structure have been identified in Fig. 19. Each color indicates the intensity of XPS and Auger peaks of an atom.
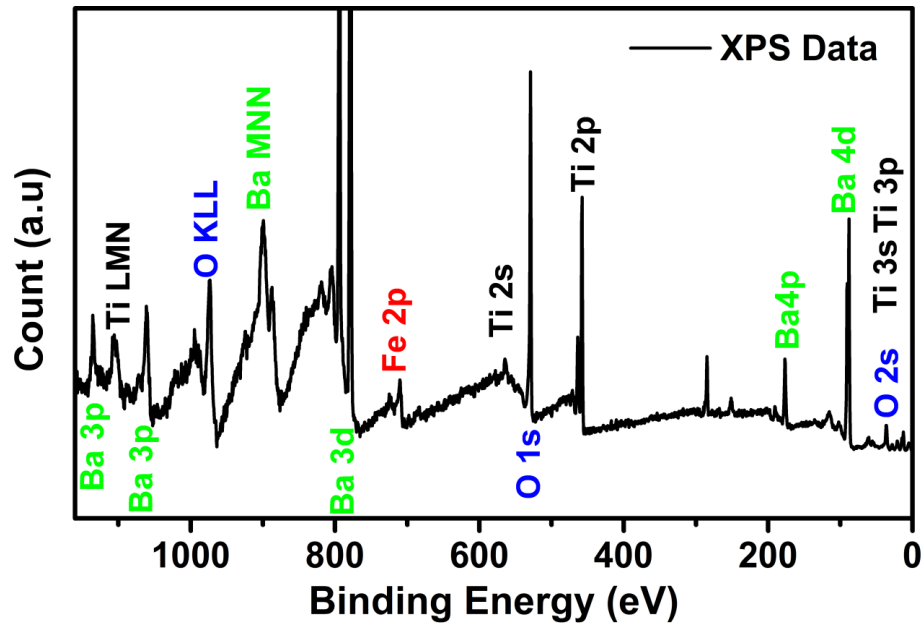

Figure 19: Background subtracted XPS scan of the BaTiO3/Iron Oxide CSNPs

High-resolution scan data from the Fe 2p orbital are plotted in Fig. 20. No shoulder in the Fe $2p^{3/2}$ rules out the possibility of metal phase in the sample. No satellites of Fe^{3+} or Fe^{2+} was found in the scan. Considering the nanoscale coating, maghemite (only Fe^{3+}) should be the thermodynamically stable structure(Birkner and Navrotsky, 2017). Considering the indication of the inverse spinel phase from XRD, XPS Fe $2p^{3/3}$have been fitted with maghemite deconvoluted peaks from the literature(Grosvenor et al., 2004). ¾ and ¼ of the Fe atoms are coordinated in octahedral and tetrahedral position in the Υ-Fe_2O_3structure. Surface and satellite peaks were not considered during the deconvolution of the Fe $2p^{3/2}$ orbital XPS data. The binding energy between the peak 2 and 3 indicates the presence of maghemite. All the peaks are deconvoluted using Gaussian parameters. We used Origin 8.5 Pro for fitting the Fe $2p^{3/2}$ peaks. Shirley backgrounds were subtracted using CASA.
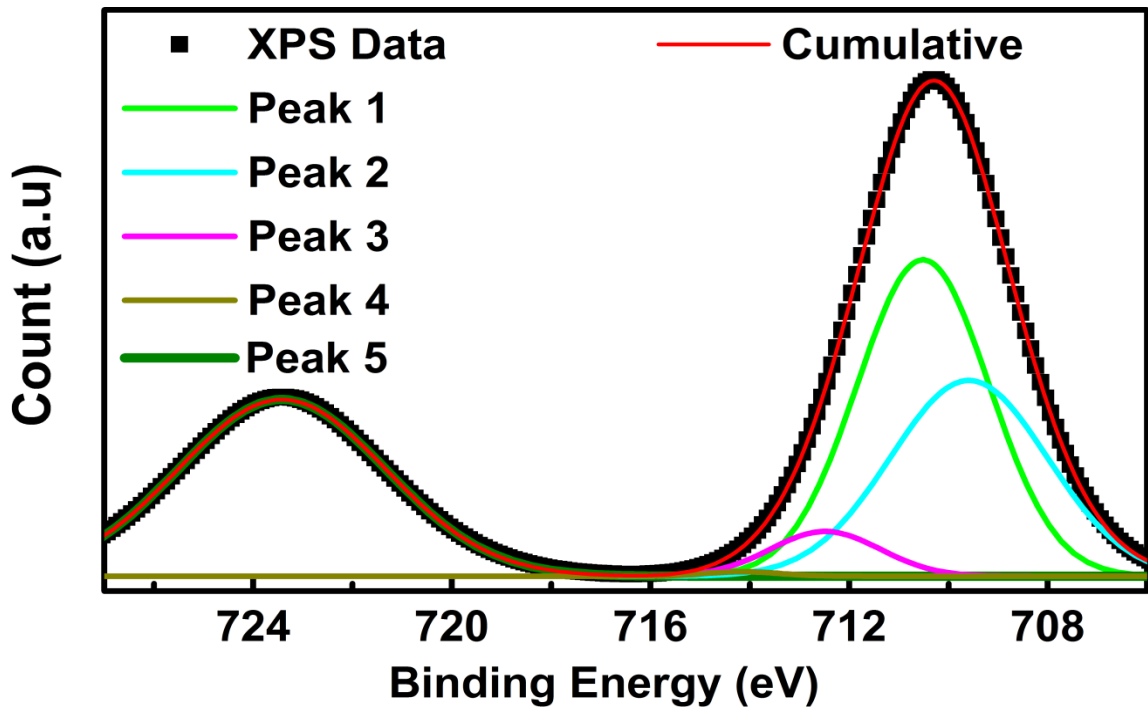

Figure 20: Sherley background subtracted HR Scan data of the Fe 2p3/2 orbital deconvoluted without surface peaks

Lower FWHM value of the peak 1-4 in the tbl. 9 supports the ϒ-Fe_2O_3 presence in the structure. Around 13 eV binding energy difference between the 3/2 and ½ orbital agree with the XPS data of the typical iron oxide.

Table 9: Deconvoluted Gaussian peak parameters of the peak 1-5 from Fig. 20

Name	Position (eV)	Area	FWHM
Peak1	710.5126	352.9095	3.12362
Peak2	709.5909	260.5075	3.72701
Peak3	712.4837	41.63253	2.6034
Peak4	714.143	2.90822	2.90822
Peak5	723.4224	310.1352	4.91504

Conclusion

Synthesize magnetoelectric BaTiO3/ Iron oxide core CSNPs are a promising material for coupling devices. Iron oxide surface nanolayer is ideal for structural as well as magnetic tuning through surface treatment like annealing in reducing ambient. Claimed clean synthesis is supported by bulk (XRD) and surface (XPS) measurements. Details XPS analysis in the literature may become helpful for analysis similar iron oxide surface structures. Expected superparamagnetic response due to the thin nanolayer of iron oxide has a wide variety of device applications.

CONCLUSION

Multifunctional TMO CSNPs have been successfully developed and characterized in this article. The varying magnetic response in the ML CSNPs in the paper 1 is expected to improve the performances of the existing bio-imaging and the targeted drug delivery technology. Detailed phase detection between the maghemite and the magnetite phase explains the differences in the magnetic responses between the oxidized and reduced CSNPs. Change in the key parameters (temperature, pressure, and size) during the oxidation/reduction process can further tune the CSNPs to meet the application-oriented specs. Uniformity in the coating and dispersion of the ME CSNPs in the paper 2 is advantageous for the multiferroic applications. Uniform thin iron oxide surface structure is ready for the medication upon treatment to meet the application requirement. Coupling between the magnetoelectric materials may substitute the exciting silicon technology and overcome the theoretical size limit of the existing technology. Multifunctional properties in the CSNPs in paper 1 and 2 may be significantly changed by introducing the quantum size effects upon reducing the core size.

REFERENCES

Baraldi, A. Structure and Chemical Reactivity of Transition Metal Surfaces as Probed by Synchrotron Radiation Core Level Photoelectron Spectroscopy. *J. Phys. Condens. Matter* **2008**, *20* (9), 93001.

Biesinger, M. C.; Payne, B. P.; Grosvenor, A. P.; Lau, L. W. M.; Gerson, A. R.; Smart, R. S. C. Resolving Surface Chemical States in XPS Analysis of First Row Transition Metals, Oxides and Hydroxides: Cr, Mn, Fe, Co and Ni. *Appl. Surf. Sci.* **2010**, *257*, 2717–2730.

Birkner, N.; Navrotsky, A. Thermodynamics of Manganese Oxides: Sodium, Potassium, and Calcium Birnessite and Cryptomelane. *Proc. Natl. Acad. Sci. U. S. A.* **2017**, *114* (7), E1046–E1053.

Blaney, L. Lehigh Preserve Magnetite (Fe3O4): Properties, Synthesis, and Applications. **2007**, *15*.

Brink, J. Transition Metal Oxides: Travels in One Dimension. *Nat. Mater.* **2006**, *5* (6), 427–428.

Bu, A. Iron Oxide Nanoparticles, Characteristics and Applications | Sigma-Aldrich http://www.sigmaaldrich.com/technical-documents/articles/technology-spotlights/iron-oxide-nanoparticles-characteristics-and-applications.html (accessed May 3, 2017).

Camarda, P.; Messina, F.; Vaccaro, L.; Agnello, S.; Buscarino, G.; Schneider, R.; Popescu, R.; Gerthsen, D.; Lorenzi, R.; Gelardi, F. M.; et al. Luminescence Mechanisms of Defective ZnO Nanoparticles. *Phys. Chem. Chem. Phys.* **2016**, *18* (18), 16237–16244.

Cho, N.-H.; Cheong, T.-C.; Min, J. H.; Wu, J. H.; Lee, S. J.; Kim, D.; Yang, J.-S.; Kim, S.; Kim, Y. K.; Seong, S.-Y. A Multifunctional Core–shell Nanoparticle for Dendritic Cell-Based Cancer Immunotherapy. *Nat. Nanotechnol.* **2011**, *6* (10), 675–682.

Grosvenor, A. P.; Kobe, B. A.; Biesinger, M. C.; McIntyre, N. S. Investigation of Multiplet Splitting of Fe 2p XPS Spectra and Bonding in Iron Compounds. *Surf. Interface Anal.* **2004**, *36* (12), 1564–1574.

Hudson, S.; Grbic, M.; Hutter, J.; Physics, A.; Ontario, W. Novel Natural Nanomaterial Spins off from Spider-Mite Genome Sequencing. **2013**, No. May, 1–2.

Janotti, A.; Van De Walle, C. G. Native Point Defects in ZnO. *Phys. Rev. B - Condens. Matter Mater. Phys.* **2007**, *76* (16).

Kargol, A.; Malkinski, L.; Caruntu, G. Biomedical Applications of Multiferroic Nanoparticles. *Adv. Magn. Mater.* **2012**, 89–118.

Khan, K.; Rehman, S.; Rahman, H. U.; Khan, Q. Synthesis and Application of Magnetic

Nanoparticles. In *Nanomagnetism*; Maria, J., Estevez, G., Eds.; One Central Press (OCP), 2014; pp 135–169.

Kim, W.; Suh, C.-Y.; Cho, S.-W.; Roh, K.-M.; Kwon, H.; Song, K.; Shon, I.-J. A New Method for the Identification and Quantification of Magnetite–maghemite Mixture Using Conventional X-Ray Diffraction Technique. *Talanta* **2012**, *94*, 348–352.

Klein, D. H.; Andren, A. W.; Carter, J. A.; Entergy, J. F.; Feldman, C.; Fulkerson, W.; Lyon, W. S.; Ogle, J. C.; Talmi, Y.; Hook, R. I. Van; et al. X-Ray Photoelectron Spectroscopic Studies of Iron Oxides The Formation of a Variety of Ferrous and Ferric Oxides and Hydroxides Is Possible during the Aqueous Corrosion of Iron. *N.Y. Sci. Environ. Sci. Technol* **1975**, *9* (22), 336–973.

Leiter, F.; Alves, H.; Pfisterer, D.; Romanov, N. G.; Hofmann, D. M.; Meyer, B. K. Oxygen Vacancies in ZnO. *Phys. B Condens. Matter* **2003**, *340–342*, 201–204.

Liu, K. W.; Chen, R.; Xing, G. Z.; Wu, T.; Sun, H. D. Photoluminescence Characteristics of High Quality ZnO Nanowires and Its Enhancement by Polymer Covering. *Appl. Phys. Lett.* **2010**, *96* (2), 23111.

Lorenz, M.; Ramachandra Rao, M. S.; Venkatesan, T.; Fortunato, E.; Barquinha, P.; Branquinho, R.; Salgueiro, D.; Martins, R.; Carlos, E.; Liu, A.; et al. The 2016 Oxide Electronic Materials and Oxide Interfaces Roadmap. *J. Phys. D. Appl. Phys.* **2016**, *49* (43), 433001.

Morrish, A.; Haneda, K. NON-COLLINEARITY AS A CRYSTALLITE-SIZE EFFECT OF γ-Fe2O3 SMALL PARTICLES. *J. Phys. Colloq.* **1980**, *41* (C1), 1–171.

Niederdraenk, F.; Luczak, P.; Seufert, K.; Kumpf, C.; Neder, R.; Dembski, S.; Graf, C.; Rühl, E.; Umbach, E. X-ray diffraction on core-shell nanoparticles for a precise structure determination (accessed May 28, 2017). http://hasyweb.desy.de/science/annual_reports/2006_report/part1/contrib/44/17976.pdf

Petrova, R. (University of C. F. QUANTITATIVE HIGH-ANGLE ANNULAR DARK FIELD SCANNING TRANSMISSION ELECTRON MICROSCOPY FOR MATERIALS SCIENCE, University of Central Florida, 2006.

Rao, C. N. R. Transition Metal Oxides. *Annu. Rev. Phys. Chem.* **1989**, *40* (1), 291–326.

Rasmussen, J. W.; Martinez, E.; Louka, P.; Wingett, D. G. Zinc Oxide Nanoparticles for Selective Destruction of Tumor Cells and Potential for Drug Delivery Applications. *Expert Opin. Drug Deliv.* **2010**, *7* (9), 1063–1077.

Reynolds, D. C.; Look, D. C.; Jogai, B.; Morkoç, H. Similarities in the Bandedge and Deep-Centre Photoluminescence Mechanisms of ZnO and GaN. *Solid State Commun.* **1997**, *101* (9), 643–646.

Rietveld, H. M.; IUCr. A Profile Refinement Method for Nuclear and Magnetic

Structures. *J. Appl. Crystallogr.* **1969**, *2* (2), 65–71.

Rodnyi, P. A.; Khodyuk, I. V. Optical and Luminescence Properties of Zinc Oxide. *Orininal text Publ. Opt. Spectrosc.* **2011**, *111* (5), 776–785.

Salaheldeen Elnashaie, S.; Danafar, F.; Hashemipour Rafsanjani, H. *Nanotechnology for Chemical Engineers*; Springer Singapore: Singapore, 2015.

Sato-Berrú, R. Y.; Vázquez-Olmos, A.; Fernández-Osorio, A. L.; Sotres-Martínez, S. Micro-Raman Investigation of Transition-Metal-Doped ZnO Nanoparticles. *J. Raman Spectrosc.* **2007**, *38* (9), 1073–1076.

Silambarasan, M.; Saravanan, S.; Soga, T. Effect of Fe-Doping on the Structural, Morphological and Optical Properties of ZnO Nanoparticles Synthesized by Solution Combustion Process. *Phys. E Low-Dimensional Syst. Nanostructures* **2015**, *71*, 109–116.

Smith, D. J. Chapter 1. Characterization of Nanomaterials Using Transmission Electron Microscopy; Royal Society of Chemistry, 2015; pp 1–29.

Sreenivasulu, G.; Popov, M.; Chavez, F. A.; Hamilton, S. L.; Lehto, P. R.; Srinivasan, G. Controlled Self-Assembly of Multiferroic Core-Shell Nanoparticles Exhibiting Strong Magneto-Electric Effects. *Appl. Phys. Lett.* **2014**, *104* (5).

Talam, S.; Karumuri, S. R.; Gunnam, N. Synthesis, Characterization, and Spectroscopic Properties of ZnO Nanoparticles. *ISRN Nanotechnol.* **2012**, *2012*, 1–6.

Teja, A. S.; Koh, P. Y. Synthesis, Properties, and Applications of Magnetic Iron Oxide Nanoparticles. *Progress in Crystal Growth and Characterization of Materials*. 2009, pp 22–45.

Thandavan, T. M. K.; Gani, S. M. A.; San Wong, C.; Md Nor, R. Enhanced Photoluminescence and Raman Properties of Al-Doped ZnO Nanostructures Prepared Using Thermal Chemical Vapor Deposition of Methanol Assisted with Heated Brass. *PLoS One* **2015**, *10* (3), e0121756.

Vempati, S.; Mitra, J.; Dawson, P. One-Step Synthesis of ZnO Nanosheets: A Blue-White Fluorophore. *Nanoscale Res. Lett.* **2012**, *7* (1), 470.

Venkatesan, T. Pulsed Laser Deposition—invention or Discovery? *J. Phys. D. Appl. Phys.* **2014**, *47* (3), 34001.

Wang, W.; Howe, J. Y.; Gu, B. Structure and Morphology Evolution of Hematite (α-Fe$_2$O$_3$) Nanoparticles in Forced Hydrolysis of Ferric Chloride. *J. Phys. Chem. C* **2008**, *112* (25), 9203–9208.

Willander, M.; Nur, O.; Sadaf, R.; Qadir, M. I.; Zaman, S.; Zainelabdin, A.; Bano, N.; Hussain, I. Luminescence from Zinc Oxide Nanostructures and Polymers and Their Hybrid Devices. *Materials (Basel).* **2010**, *3*, 2643–2667.

Wuhrer, R.; Moran, K. Low Voltage Imaging and X-Ray Microanalysis in the SEM: Challenges and Opportunities. *Mater. Sci. Eng* **2016**, *109*.

Zhang, J. Spectroscopic Techniques for Studying Optical Properties of Nanomaterials. In *Optical Properties and Spectroscopy of Nanomaterials*; WORLD SCIENTIFIC, 2009a.

Zhang, J. Z. *Optical Properties and Spectroscopy of Nanomaterials*; World Scientific Publishing Co. Pte. Ltd.: Singapore, 2009b.

Zhang, Y.; Nayak, T. R.; Hong, H.; Cai, W. Biomedical Applications of Zinc Oxide Nanomaterials. *Curr. Mol. Med.* **2013**, *13* (10), 1633–1645.

Zhao, S.; Shifeng. Advances in Multiferroic Nanomaterials Assembled with Clusters. *J. Nanomater.* **2015**, *2015*, 1–12.

History and Development of Nanomaterials http://www.azonano.com/article.aspx?ArticleID=3393 (accessed Apr 27, 2017).

Nanotechnology Timeline | Nano https://www.nano.gov/timeline (accessed Apr 27, 2017).

NASA - Honeycomb Carbon Crystals Possibly Detected in Space.